Check for updates

JAMES | Journal of Advances in Modeling Earth Systems

RESEARCH ARTICLE
10.1029/2023MS003957

Analytic Parameterization of Longwave Optical Properties of Bulk Vegetation Layer Permitting Non-Zero Leaf Reflectivity and Its Implementation in CLM5

Hyeon-Ju Gim[1] and Seon Ki Park[2,3]

[1]Numerical Modeling Group, Korea Institute of Atmospheric Prediction Systems, Seoul, Korea, [2]Department of Climate and Energy Systems Engineering, Ewha Womans University, Seoul, Korea, [3]Center for Climate/Environment Change Prediction Research, Ewha Womans University, Seoul, Korea

Key Points:

- A new scheme considers leaf reflection when deriving vegetation layer longwave optical properties for land surface model
- Despite its simplicity, the new scheme demonstrates accuracy comparable to expensive numerical multi-layer radiative transfer model
- The new scheme generates land surface emissivity values exhibiting greater agreements with satellite retrievals compared to previous schemes

Correspondence to:

S. K. Park,
spark@ewha.ac.kr

Citation:

Gim, H.-J., & Park, S. K. (2024). Analytic parameterization of longwave optical properties of bulk vegetation layer permitting non-zero leaf reflectivity and its implementation in CLM5. *Journal of Advances in Modeling Earth Systems*, *16*, e2023MS003957. https://doi.org/10.1029/2023MS003957

Received 1 AUG 2023
Accepted 11 AUG 2024

Author Contributions:

Conceptualization: Hyeon-Ju Gim
Data curation: Hyeon-Ju Gim
Formal analysis: Hyeon-Ju Gim
Funding acquisition: Seon Ki Park
Investigation: Hyeon-Ju Gim
Methodology: Hyeon-Ju Gim
Project administration: Seon Ki Park
Resources: Hyeon-Ju Gim
Software: Hyeon-Ju Gim
Supervision: Seon Ki Park
Validation: Hyeon-Ju Gim
Visualization: Hyeon-Ju Gim
Writing – original draft: Hyeon-Ju Gim
Writing – review & editing: Seon Ki Park

© 2024 The Author(s). Journal of Advances in Modeling Earth Systems published by Wiley Periodicals LLC on behalf of American Geophysical Union. This is an open access article under the terms of the Creative Commons Attribution-NonCommercial-NoDerivs License, which permits use and distribution in any medium, provided the original work is properly cited, the use is non-commercial and no modifications or adaptations are made.

Abstract For modern land surface models (LSMs) representing a singular bulk vegetation layer, the longwave optical properties (i.e., emissivity, reflectivity, and transmittivity) of vegetation layer are derived with a simplified constraint of assuming zero leaf reflectivity. This constraint is necessary, for instance, to the Beer–Lambert (B–L) law to establish a relationship between the optical properties and leaf area index. However, the simplified constraint leads to an overestimation of land surface emissivity in the vegetated regions. In this study, we introduce a new scheme considering realistic leaf reflectivity values rather than assuming zero. This new scheme is based on the relationship derived from the B–L law, but it is statistically augmented to consider the effects of leaf reflections. It is designed to emulate a multi-vegetation-layer numerical model known as the Norman model, which is capable of numerical calculations of multi-reflections among leaves. This new method consists of only a couple of simple equations; despite its simplicity, it very closely mimics the Norman model; The discrepancy of the results between the new method and the Norman model is less than measurement uncertainties for any combination of input parameters. When the new scheme is implemented in the Community Land Model version 5 (CLM5), the land surface emissivity values are simulated much more consistently with global measurements, resulting in significant alterations of land surface energy budget. The enhanced realism through our new scheme is poised to contribute to more accurate numerical weather and climate simulations.

Plain Language Summary In many state-of-the-art land surface models (LSMs), vegetation is represented as a single layer overlying the ground. In calculations for land surface processes, it is essential to determine the emissivity, reflectivity, and transmittivity of a vegetation layer; these properties for longwave radiation are, typically, either calculated using a simple function that relates them to the leaf area index or are prescribed to be constants. All these methods utilized a simplified constraint of zero leaf reflectivity, resulting in an apparent overestimation of the land surface emissivity over vegetated surface. In this study, a new method is developed to eliminate the simplified constraint and to consider leaf reflections. The new method is designed to be simple, having only a couple of simple equations, but involving the effect of multiple reflections of radiative beams among leaves. When the new method is applied to an LSM with realistic values of leaf reflectivity, the LSM yields much more accurate global patterns of land surface emissivity, accompanied by significant changes in land surface energy balance. Owing to its simplicity, this method is expected to be applied readily to various LSMs, potentially contributing to enhanced realism of weather and climate simulations.

1. Introduction

Land surface models (LSMs) have been developed to provide physically reliable lower boundary conditions to atmosphere for climate projection and weather prediction models (Dickinson et al., 1998; Manabe, 1969; Sellers et al., 1986). In the last few decades, LSMs have evolved to include more geophysical processes that are data-driven and/or theoretically robust to achieve physical coherence with the observations (Fisher & Koven, 2020; Pitman, 2003; Sellers et al., 1997). Among those processes, longwave (or thermal infrared) radiative processes on land surface are crucial in LSMs for calculating land surface energy budget and land surface temperatures. The optical properties that govern these longwave processes are primarily determined by prescription or derivation, depending on the diverse land surface materials and structures (Jin et al., 1997; Zhou et al., 2003).

The literature highlights that choosing to prescribe or derive the land surface emissivity (ε_{land}) in LSM can lead to to significant differences in climate simulations. Jin and Liang (2006) explored the effects of prescribing observed

19422466, 2024, 9, Downloaded from https://agupubs.onlinelibrary.wiley.com/doi/10.1029/2023MS003957 by Ewha Womans University Library, Wiley Online Library on [04/03/2025]. See the Terms and Conditions (https://onlinelibrary.wiley.com/terms-and-conditions) on Wiley Online Library for rules of use; OA articles are governed by the applicable Creative Commons License

value of ε_{land} (i.e., ∼0.90), as opposed to the default value of 0.96, specifically in arid (non-vegetated) regions employing an LSM of the Community Land Model version 2 (CLM2). The findings indicated that the differences in ε_{land} led to changes in radiational and turbulent land surface fluxes by 2–5 Wm^{-2} over the specified arid regions. Similarly, in sensitivity tests conducted by Luo et al. (2023) and Ma et al. (2019) using CLM5 with varying canopy vegetation emissivity, their results demonstrated that increased emissivity led to a warming effect on soil temperature at depths greater than 1.6-m by ∼1°C in frozen soil regions, accompanied by significant alterations in land surface fluxes.

The methods for addressing longwave land optical parameters have evolved; however, there is still an opportunity for further enhancement, particularly in the case of for high-complexity LSMs. The initial global LSM—introduced by Manabe (1969) and referred to as the Manabe model—simplistically treated land surface as an opaque solid surface for longwave radiative processes. This LSM relies just one parameter, ε_{land}, for longwave processes, and it is globally prescribed with a constant value of unity. Considering the variations in the ε_{land} depending on the physical trait of plants (Feltz et al., 2018; Van de Griend & Owe, 1993), prescribing realistic or measured values is regarded as a straightforward method to enhance the realism of longwave processes in LSMs.

However, the prescription of the measured ε_{land} is applicable only to the LSMs whose land surface is represented as a singular bulk surface. This bulk surface represents both soil surface and vegetation layer, which are blended considering land surface parameters. LSMs utilizing this blended singular bulk surface include the Manabe model (Manabe, 1969), the Noah LSM (Ek et al., 2003), the Joint UK Environment Simulator (JULES; Best et al., 2011), and the ORganizing Carbon and Hydrology In Dynamic EcosystEms (ORCHIDEE, Krinner et al., 2005).

On the other hand, the prescription method is not theoretically applicable to the LSMs with higher complexity, particularly those with vegetation canopy is explicitly represented, separately from the ground or soil surface. Such complex LSMs include the CLM (D. M. Lawrence et al., 2019), the Canadian LAnd Surface Scheme (CLASS; Verseghy, 2012), the Community Atmosphere-Biosphere-Land Exchange (CABLE; Wang et al., 2011), Geophysical Fluid Dynamics Laboratory's land model (LM; Zhao et al., 2018), and the Noah LSM with Multi-Parameterization options (Noah-MP; Niu et al., 2011). These LSMs have a structure of two overlapping-planes in the perspective of longwave radiation processes: (a) an opaque ground surface and (b) an overlaying semi-transparent single layer of plant canopy. In this framework, ε_{land} is not a parameter to be prescribed but rather a variable derived diagnostically from the canopy vegetation layer emissivity (ε_{cano}), reflectivity (ρ_{cano}), and transmittivity (τ_{cano}), along with the ground emissivity (ε_{grnd}).

The value of ε_{cano} increases as canopy layer thickens optically or, more specifically, as leaf area index (L) of the layer increases (Feltz et al., 2018; Francois et al., 1997; Pérez-Planells et al., 2019; Van de Griend & Owe, 1993). The value is near zero when the layer is very thin, and as the layer thickens it increases approaching a certain point of an upper limit at which the canopy layer thickens enough to be opaque. Francois et al. (1997) showed via theoretical model experiments that the upper limit of ε_{cano} is unity when the scattering elements (e.g., leaves) are reflectionless. This is because the radiative beam that incident onto canopy layer is entirely trapped like blackbody when a canopy layer is dense (or L is large) enough to be opaque. When the scattering elements are able to reflect the incident beam, the ε_{cano} becomes less than unity. In Francois et al. (1997), various values of the leaf reflectivity (ρ_{leaf}) are tested, and the larger the prescribed ρ_{leaf} is, the lower the upper limit of ε_{cano} appears.

According to literature on spectroscopy, it is apparent that a significant fraction of the longwave beam incident onto leaves are reflected backward. Richardson et al. (2021), for instance, described that the values of ρ_{leaf} range from 0.03 to 0.08 depending on the plant species and its developmental stage, which values were determined by sophisticated laboratory measurements. These realistic values of ρ_{leaf} need to be considered to parameterize the optical properties of the bulk canopy layer in LSMs, but its effect of reflectiveness has not been fully parameterized in any state-of-the-art LSM.

In CLASS, ε_{cano} is simply fixed at unity (hence, ρ_{cano} and τ_{cano} are zero) globally (Verseghy, 2012). In LM, ε_{cano}, ρ_{cano}, and τ_{cano} are fixed to vegetation-type-specific values and are prescribed such that the dependency of these parameters on L does not be represented. In CLM and Noah-MP, ε_{cano} is described as a simple singular equation of L, which is based on the Beer−Lambert (B−L) law; however, this equation is only valid for and is constrained to $\rho_{leaf} = 0$. This is because the B−L law does not consider the multi-reflections among leaves. In CABLE, the changes in ε_{cano}, according to ρ_{leaf} and L, are considered by calculating the radiometric emissions from the canopy

19422466, 2024, 9, Downloaded from https://agupubs.onlinelibrary.wiley.com/doi/10.1029/2023MS003957 by Ewha Womans University Library, Wiley Online Library on [04/03/2025]. See the Terms and Conditions (https://onlinelibrary.wiley.com/terms-and-conditions) on Wiley Online Library for rules of use; OA articles are governed by the applicable Creative Commons License

layer; however, ρ_{leaf} is constrained to be zero for the radiometric response of the beam incident onto the canopy layer (namely, there is no reflection for the longwave beam incident onto the canopy layer) (Wang et al., 2011).

Based on the B−L law, the changes in the optical parameters according to L can be described well with a simple equation (Monsi, 1953). This equation requires a simplistic assumption of zero value of ρ_{leaf}, and this assumption inevitably results in overestimated ε_{land} for vegetation-covered regions. For example, ε_{land} is calculated to be unity (or 0.9999 before rounding off) when it is calculated by the method used in CLM5 for forest covered surface with $L = 3$ (whose value is moderate in the mid-latitude in summer). Measurements of ε_{land} in the various literature, on the contrary, are significantly less than unity for various land surface types (Arp & Phinney, 1980; Feltz et al., 2018; Pérez-Planells et al., 2019; Van de Griend & Owe, 1993). For instance, the observational values of the ε_{land} are shown to be near 0.97 for densely vegetated regions, including the Amazon and the Corn Belt regions as the values are derived by a state-of-the-art satellite retrieval system, called the Combined ASTER (Advanced Spaceborne Thermal Emission and Reflection Radiometer) and MODIS (Moderate Resolution Imaging Spectroradiometer) Emissivity over Land (CAMEL, Feltz et al., 2018).

For the consideration of realistic ρ_{leaf}, the Norman model (Norman, 1979) can be an adequate alternatives. This model has been widely used for terrestrial ecosystem models with multiple vegetation layers, including CANOAK (Baldocchi & Harley, 1995) and the Soil–Plant–Atmosphere model (SPA; Williams et al., 1996). In the Norman model, ρ_{leaf} is not constrained to be zero; this model can consider the multi-reflections among leaves with a prescribed value of ρ_{leaf}, not requiring the assumption of no reflectiveness. On the other hand, this model has disadvantages that it is computationally too expensive and cumbersome to be implemented for LSMs in which the canopy is represented as a singular bulk layer. This is because, this model should be solved numerically with multiple canopy layers, for which a recommended practice suggests employing a few tens of vegetation layers (Bonan, 2019).

For this study, we developed an alternative method that was designed for easy implementation in LSMs while incorporating enhanced relationships between the canopy layer bulk properties (ε_{cano}, ρ_{cano}, and τ_{cano}) and L. This method takes into account the effects of multi-reflections among leaves for given values of ρ_{leaf}. This new method employs a couple of simple equations, and, despite its simplicity, it very accurately emulates the Norman model. To assesses its benefits within LSMs, the new method is implemented in a widely used-LSM of CLM5, investigating the effects of vegetation layer longwave reflections. In Sections 2 and 3, we present the strategy and processes of the new model development. Section 4 introduced brief results from the implementation of the new method to CLM5. Section 5 comprises a summary and discussion.

2. Methodology for Designing a New Scheme

The B–L law-based analytic solution, employed in several LSMs as mentioned earlier, allows for determining the values of τ_{cano} (or ε_{cano}) according to corresponding L value; however, this solution requires assuming a zero value for ρ_{leaf}, resulting in an unrealistic zero value for ρ_{cano}. The new scheme developed in this study can be described as an analytic parameterization. It builds upon the B–L law analytic solution, and it is augmented to account for variations in τ_{cano} and ρ_{cano} based on ρ_{leaf} as well as their changes according to the L; the effects of different ρ_{leaf} values are quantified using the Norman model numerical solution, providing guidance for designing the new formula. Specifically, the new scheme was developed to retain the simplicity of the B–L law analytic solution, while incorporating the physical generality of the Norman model numerical solution. The seamless integration of these two models is primarily facilitated by the fact that they both share the same theoretical modeling framework. For example, they yield identical results for the case of reflectionless leaves. A comprehensive description of Norman model and its linkage to B–L law is described in Appendix A. The characteristics of each method are summarized in Table 1, and the developed schemes with determined parameters are represented in Table 3 (refer to later section).

2.1. A New Scheme for Bulk Canopy Layer τ_{cano} and ρ_{cano}

For the development of the new equation, efforts were made to modify Equation A5—the B–L law analytic solution—to incorporate the effects of leaf reflection, especially when the ρ_{leaf} has a significant value (It is noteworthy that in the new scheme the K_d in Equation A5 is set to zero, assuming that a vegetation layer consists of horizontally oriented leaves distributed random, similar to the B–L law analytic solution utilized in CLM and Noah-MP). This scheme consists of two equations, each designed to derive the τ_{cano} and ρ_{cano}, respectively.

Table 1
Brief Characteristics of Longwave Process Methods

	B–L law equation	Norman model	New scheme
Solution type	Analytic	Numerical (iteration or tridiagonal matrix needed)	Semi-analytic
First output	**Bulk optical properties of canopy layer**[a]	Irradiance on canopy layers[b]	**Bulk optical properties of canopy layer**[a]
Multi-reflections	Not considered	**Considered**	**Considered**
Cost/simplicity	**Cheap/simple**	Expensive/complicated	**Cheap/simple**
Reference	Monsi (1953) and Sellers et al. (1986)	Norman (1979) and Bonan (2019)	This study

Note. The same properties of new scheme and existing schemes are highlighted in bold. [a]Namely, canopy layer bulk emissivity (ε_{cano}), reflectivity (ρ_{cano}), and transmittivity (τ_{cano}). [b]From which the optical properties of the bulk canopy layer can be calculated.

The τ_{cano} can be interpreted, according to Equation A4, as remaining portion of the incident irradiance after N-times-attenuation of $\varepsilon_{leaf}\Delta L$ as it passes through N thin vegetation layers. In addition, the τ_{cano} should increases when ρ_{leaf} becomes greater than zero with τ_{leaf} remaining unchanged. This is because a certain portion of reflected beam can penetrate the entire vegetation layer during multi-reflection among multi-layers of leaves. Hence, a coefficient, C_ρ, was introduced to quantify the effect of leaf reflection on the penetration. This coefficient can be interpreted as the effective ratio of returning and penetrating radiance against the one reflected on a vegetation layer including leaves with ΔL area. It ranges zero to unity; zero C_ρ indicates that all radiation reflected on a small surface fully penetrates the layer, while unity C_ρ indicating none of them penetrating the layer. The new equation for τ_{cano} is designed as follows:

$$\tau_{cano} = \exp\left(-\left(\varepsilon_{leaf} + C_\rho \rho_{leaf}\right) L\right) \tag{1}$$

Note that Equation 1 is identical to Equation A5 when ρ_{leaf} is constrained to be zero (i.e., assuming reflectionless leaves).

On the other hand, for deriving the ρ_{cano}, the other new equation is designed as follows in Equation 2 based on a few inherent properties of the relationship between ρ_{cano} and L: (a) ρ_{cano} is zero when L is zero; (b) ρ_{cano} increases with L; and (c) when L is large enough for the layer to be opaque, ρ_{cano} increases with L, but saturates at a certain upper limit (say, $\rho_{cano,max}$). Additionally, it is assumed that the changes in ρ_{cano} according to L can be described by a certain value of the extinction coefficient (K_ρ) for a given conditions of the physical properties of the canopy. With these two new parameters ($\rho_{cano,max}$ and K_ρ), the new equation is designed as follows:

$$\rho_{cano} = \rho_{cano,max}\left(1 - \exp(-K_\rho L)\right) \tag{2}$$

Therefore, the new scheme is composed of Equations 1 and 2, whose three new parameters—C_ρ, $\rho_{cano,max}$, and K_ρ are needs to be determined to relevantly emulate the Norman model. To this end, many sets of the bulk canopy layer optical properties are calculated by the Norman model with various combinations of the input conditions of L and leaf optical properties.

2.2. Input Parameters and Simulations of Norman Model

An LSM does not need to cover the mathematically available full range of the land surface properties, but it needs to cover just a practical range for the globe within which the measured values are included. Literature on measurements were collected for L, ε_{leaf}, and ρ_{leaf}, and the ranges wide enough to include the measurements were determined for the target coverages of the new method (Table 2); for L from 0 to 7, ρ_{leaf} from 0 to 0.1 and its corresponding range of ε_{leaf} from 0.9 to unity were selected. τ_{leaf} was set to zero (thus, $\varepsilon_{leaf} = 1 - \rho_{leaf}$), that is, leaf surface is treated as a radiatively opaque for longwave radiation. Literature on spectroscopy reports indicate that longwave radiation penetrates only a few micrometers of leaves (Chalmers, 2013), while leaves are typically thicker than 100 μm.

We calculated ε_{cano}, ρ_{cano}, τ_{cano}, and ε_{land} using the Norman model for various combinations of the inputs of L and ρ_{leaf} (or ε_{leaf}). With an interval of 0.1 for L from 0 to 7 and 0.01 for ρ_{leaf} from 0.00 to 0.10 (or its corresponding ε_{leaf}

19422466, 2024, 9, Downloaded from https://agupubs.onlinelibrary.wiley.com/doi/10.1029/2023MS003957 by Ewha Womans University Library, Wiley Online Library on [04/03/2025]. See the Terms and Conditions (https://onlinelibrary.wiley.com/terms-and-conditions) on Wiley Online Library for rules of use; OA articles are governed by the applicable Creative Commons License

19422466, 2024, 9, Downloaded from https://agupubs.onlinelibrary.wiley.com/doi/10.1029/2023MS003957 by Ewha Womans University Library, Wiley Online Library on [04/03/2025]. See the Terms and Conditions (https://onlinelibrary.wiley.com/terms-and-conditions) on Wiley Online Library for rules of use; OA articles are governed by the applicable Creative Commons License

Table 2
Ranges of Leaf Traits Measured and Addressed for the New Model Development

	Leaf area index (L)	Leaf emissivity (ε_{leaf})	Leaf reflectivity (ρ_{leaf})
Baret et al. (2006)[a]	0–6		
Bonan (2019)[b]		0.96–0.98	
Sutherland (1986)[c]		0.956	
Richardson et al. (2021)[d]			0.0385–0.0516
Target coverages of the new model	0–7	0.90–1.00	0.00–0.10

[a]Based on multiple data sets from various sources. [b]Introduced as a typical range in LSMs. [c]A broadband from 2 to 18 μm. [d]Five temperate deciduous species for a broadband from 2 to 14 μm.

from 1.00 to 0.90), a total of 70 × 11 bulk properties sets were calculated. L_i was set to 0.01 for every layer; thus, the number of layers, N, was $L \times 100$.

The first output of the Norman model is the irradiance at each canopy layer; the bulk canopy properties were derived from these values as follows:

$$\rho_{cano} = I_N^{\uparrow}/I_N^{\downarrow}, \text{with } \varepsilon_{grnd} = 1$$

$$\tau_{cano} = \frac{I_0^{\downarrow}}{I_N^{\downarrow}}$$

$$\varepsilon_{cano} = 1 - \rho_{cano} - \tau_{cano}$$

$$\varepsilon_{land} = 1 - \left(\rho_{cano} + {\tau_{cano}}^2 \times (1 - \varepsilon_{grnd})\right), \text{with } \varepsilon_{grnd} = 0.96$$

where $I_N^{\uparrow}$ and $I_N^{\downarrow}$ indicate the upward and downward irradiance above the top layer, respectively, $I_0^{\downarrow}$ is the downward irradiance below the bottom layer, and ε_{grnd} is the ground surface emissivity, which was set to 0.96 (0.96 is the default value of ε_{grnd} in the CLM5) to calculate ε_{land} and to 1 to determine ρ_{cano}.

2.3. Data Sets of Satellite Observations

A space-borne global data set of ε_{land} from CAMEL (Borbas et al., 2018; Feltz et al., 2018; Loveless et al., 2021) was utilized as the reference. The CAMEL is a state-of-the-art data set of ε_{land}, developed by fusing two different pre-existing data sets to maximize their different and complementary advantages (Borbas et al., 2018).

The monthly values of ε_{land} of the core 13 narrow-bands between 3.6 and 14.3 μm, called hinge points, were obtained from CAMEL version 2 (Hook, 2017), which was globally gridded evenly by 0.05°. Given that the

Table 3
Equations for Vegetation Layer Longwave Optical Properties in (Top) B–L Law Analytic Solution and (Middle and Bottom) Semi-Analytic (or Analytic Parameterization) Solutions Developed in This Study

Explanation	Equations
B–L law analytic solution	$\tau_{cano} = \exp(-L)$ $\rho_{cano} = 0$
Semi-analytic solution with simplified coefficients	$\tau_{cano} = \exp(-L)$ $\rho_{cano} = \frac{\rho_{leaf}}{2}(1 - \exp(-2L))$
Semi-analytic solution with best-fit coefficients	$\tau_{cano} = \exp\left(-\left(\varepsilon_{leaf} + C_\rho \rho_{leaf}\right) L\right)$ $\rho_{cano} = \rho_{cano,max}(1 - \exp(-K_\rho L))$ where $C_\rho = 1 - 0.26\,\rho_{leaf}$, $\rho_{cano,max} = 0.5037\,\rho_{leaf} - 2.3629 \times 10^{-5}$, and $K_\rho = -0.07936\,\rho_{leaf} + 2.002$

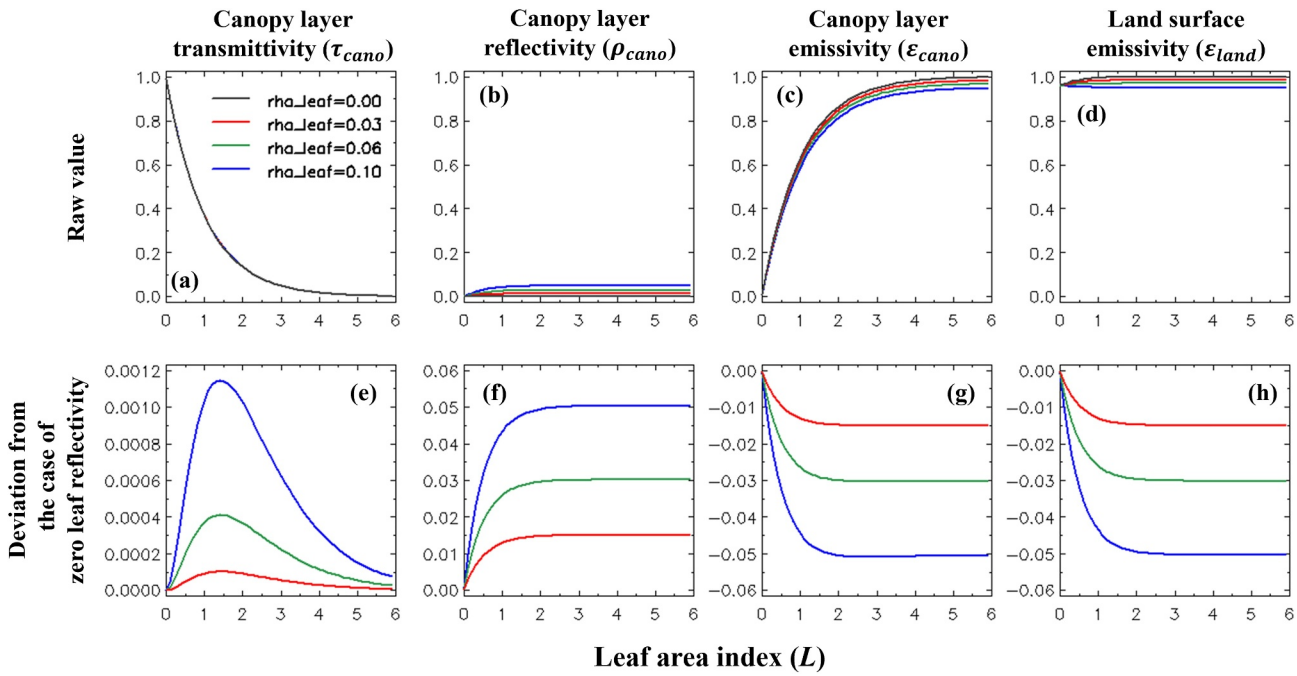


Figure 1. Bulk optical properties—canopy layer transmittivity (τ_{cano}), reflectivity (ρ_{cano}), emissivity (ε_{cano}), and land surface emissivity (ε_{land})—according to leaf area index (L) simulated using the Norman model with different inputs of leaf reflectivity (ρ_{leaf}). Upper panels (a–d) depict their raw values, while lower panels (e–h) show the deviations from the case of zero ρ_{leaf}. Ground emissivity (ε_{grnd}) was set to 0.96 to calculate ε_{land}.

spectral range of 8–13.5 μm is optimum to represent the entire spectrum of longwave radiation (Cheng et al., 2013), the provided values of the seven hinge points in this range were averaged to calculate the representative ε_{land}. For this average, each value was weighted by the Planck function at the monthly skin temperature averaged for day and night, which are provided by MOD11C3 MODIS products (Wan et al., 2021). Among the calculated ε_{land} values, only those with a quality flag reported to be "good" for both CAMEL and MOD11C3 were utilized in this study.

3. Determining the Parameters of the New Scheme

3.1. Reference Values of Bulk Optical Properties of Canopy Vegetation Layer

As the reference of the new scheme, the bulk optical properties of a canopy layer according to L were generated using the Norman model for various values of ρ_{leaf} (Figure 1). τ_{cano} exponentially decreases with an increase in L and approaches zero, resulting in τ_{cano} values of approximately 1/10, 1/100, and 1/1000 for L values of 2.3, 4.6, and 6.9, respectively (Figure 1a). On the other hand, the effects of leaf reflections on τ_{cano} are relatively insignificantly. Larger τ_{cano} values are obtained with larger values of ρ_{leaf}, but the differences are negligible, at most near 0.001 (blue line in Figure 1e).

In contrast, ρ_{cano} exhibits considerable variability with respect to the ρ_{leaf} value. As expected, ρ_{cano} remains zero for all L when ρ_{leaf} is set to zero. However, as ρ_{leaf} is assigned non-zero values, ρ_{cano} increases with L and approaches a certain upper asymptote (Figures 1b and 1f). The asymptote is close to $\rho_{leaf}/2$, but not identical. For instance, in densely vegetated cases ($L > 3$), ρ_{cano} is approximately 0.05 and 0.03 for ρ_{leaf} values of 0.1 and 0.06, respectively.

ε_{cano} increases with L and approaches unity when ρ_{leaf} is zero. However, when ρ_{leaf} is greater than zero, the saturated values of ε_{cano} becomes less than unity. The absolute magnitudes of deviations in ε_{cano} and ρ_{cano} are nearly the same for different values of ρ_{leaf}, but their directions are opposite (Figures 1f and 1g). This indicates that the leaf reflection (e.g., $\rho_{leaf} > 0$) affects ρ_{cano} and ε_{cano} in opposite directions.

19422466, 2024, 9, Downloaded from https://agupubs.onlinelibrary.wiley.com/doi/10.1029/2023MS003957 by Ewha Womans University Library, Wiley Online Library on [04/03/2025]. See the Terms and Conditions (https://onlinelibrary.wiley.com/terms-and-conditions) on Wiley Online Library for rules of use; OA articles are governed by the applicable Creative Commons License

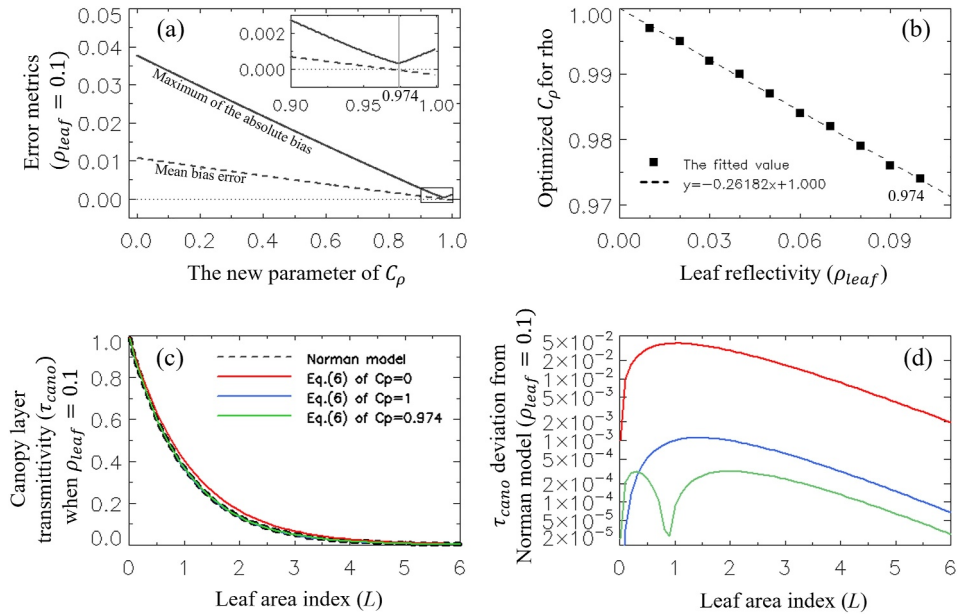


Figure 2. (a) Two error metrics for canopy layer bulk transmittivity (τ_{cano}) derived from the new scheme (Equation 1) with various values of new coefficient, C_ρ, from zero to unity when leaf reflectivity (ρ_{leaf}) is 0.1, (b) the optimized C_ρ (i.e., the C_ρ value with the lowest maximum absolute bias) with given ρ_{leaf} values from 0.01 to 0.1, (c) raw values of τ_{cano}, and (d) their deviation from the reference values (from the Norman model) according to L for a few specific values of C_ρ when ρ_{leaf} is 0.1. Error metrics in (a) were calculated using the deviations from the reference values in the Norman model, and the metrics include the mean bias error and the maximum of the absolute error for L from 0 to 6.

When L is zero, ε_{land} is equal to ε_{grnd}, and it increases with L and nearly saturates when L is greater than 2 (Figures 1d and 1h). The saturated values of ε_{land} are nearly similar to those of ε_{cano} (Figures 1c and 1d). The differences in ε_{land} according to ρ_{leaf} are nearly identical to those in ε_{cano} (Figures 1g and 1h).

3.2. Determination of the Parameter C_ρ

As mentioned in the previous section, the new scheme represented by Equations 1 and 2 has three new parameters (i.e., C_ρ, $\rho_{cano,max}$, and K_ρ) that should be determined to relevantly emulate the Norman model. This subsection describes the processes of parameter determination.

As demonstrated in Figure 1a, the profile of τ_{cano} with respect to L remains relatively consistent for different values of ρ_{leaf}. This suggests that Equation 1 with unity value of C_ρ, which is similar to Equation A6, can provide reliable results irrespective of ρ_{leaf}. To achieve more accurate quantification, various values of C_ρ from zero to unity with an interval of 0.001 were tested (Figure 2).

Figure 2a depicts the error metrics of τ_{cano} according to C_ρ for $\rho_{leaf} = 0.1$, including the mean bias error (MBE) and the maximum of the absolute errors for L from 0 to 6 (MXerr). As stated in Section 2, Equation 1 produces acceptable values of τ_{cano} when C_ρ is set to unity, but its maximum accuracy is found when C_ρ is set to 0.974 when $\rho_{leaf} = 0.1$ (Figure 2a). MXerr is ~0.001 for C_ρ of unity, and it reduces by one order of magnitude for C_ρ of 0.974 (Figure 2d).

The optimum values of the C_ρ, which minimized the MXerr, linearly decreases with ρ_{leaf} with the slope of near −0.26, from 1.0 to 0.974 for prescribed ρ_{leaf} from zero to 0.1 (Figure 2b). It is noteworthy that τ_{cano} with $C_\rho = 0$ exhibits a significant magnitude of errors (red lines in Figures 2c and 2d), and this is the case that actual values of ε_{leaf} are used in the B–L law analytic solution of Equation A5, which violates the assumption of no leaf reflection.

3.3. Determination of the Parameter $\rho_{cano,max}$

Another new parameter, $\rho_{cano,max}$, represents the asymptote (or the upper limit) for the increase in ρ_{cano} with L (see Figures 1b and 1f); thus, $\rho_{cano,max}$ is ρ_{cano} corresponding to a sufficiently large L. From the Norman model

19422466, 2024, 9, Downloaded from https://agupubs.onlinelibrary.wiley.com/doi/10.1029/2023MS003957 by Ewha Womans University Library, Wiley Online Library on [04/03/2025]. See the Terms and Conditions (https://onlinelibrary.wiley.com/terms-and-conditions) on Wiley Online Library for rules of use; OA articles are governed by the applicable Creative Commons License

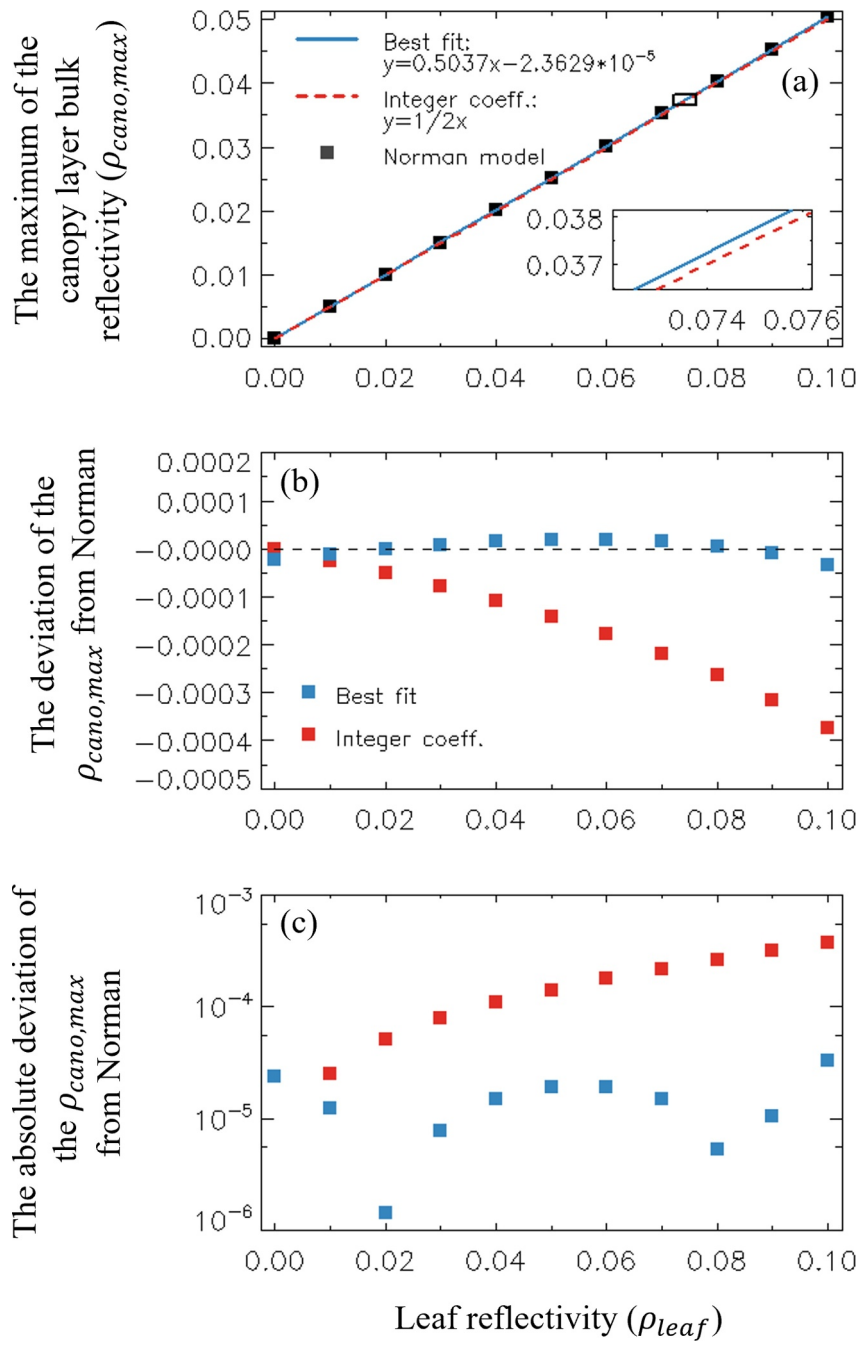


Figure 3. Maximum of canopy layer bulk reflectivity ($\rho_{cano,max}$): (a) the reference values of $\rho_{cano,max}$ (derived from the Norman model) (black squares), the two linear regression lines of $\rho_{cano,max}$ with best-fit (blue solid line) and with simplified integer coefficient (red dashed line), and (b) deviation and (c) absolute deviation of the regressed $\rho_{cano,max}$ from the reference values.

experiments, it is revealed that ρ_{cano} becomes fully saturated for L values greater than 9. Beyond this point, there is no change in ρ_{cano} by a magnitude greater than the computer truncation error (10^{-7}). ρ_{cano} for $L = 10$ derived from the Norman model were determined to be the reference values of $\rho_{cano,max}$. Thus, 10-values of $\rho_{cano,max}$ were derived from the Norman model for 10-values of ρ_{leaf} between 0.01 and 0.10 at an interval of 0.01; they are depicted in Figure 3a with the pair of zero $\rho_{cano,max}$ for zero ρ_{leaf}.

19422466, 2024, 9, Downloaded from https://agupubs.onlinelibrary.wiley.com/doi/10.1029/2023MS003957 by Ewha Womans University Library, Wiley Online Library on [04/03/2025]. See the Terms and Conditions (https://onlinelibrary.wiley.com/terms-and-conditions) on Wiley Online Library for rules of use; OA articles are governed by the applicable Creative Commons License

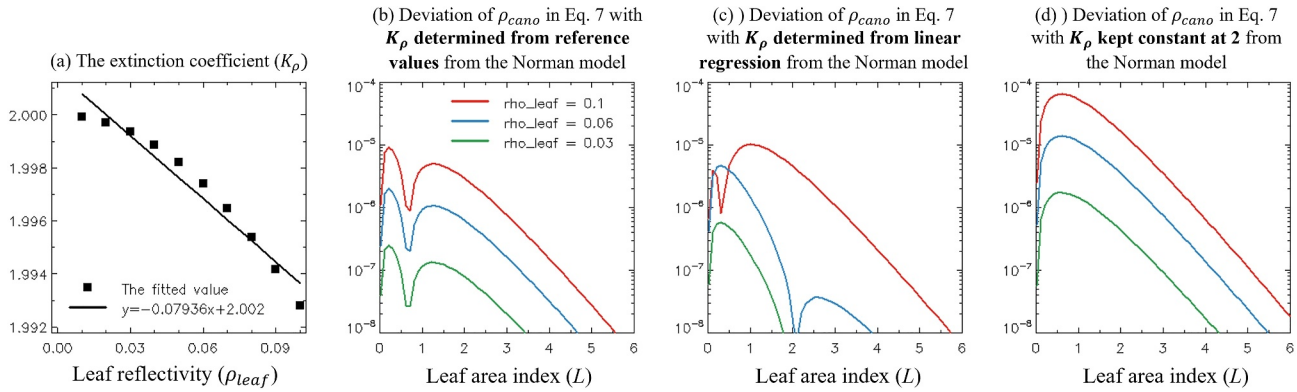


Figure 4. (a) A plot against the leaf reflectivity (ρ_{leaf}) of the extinction coefficient (K_ρ) derived by fitting Equation 2 to the Norman model simulation of the bulk canopy reflectivity (ρ_{cano}) and (b–d) the deviations of ρ_{cano} values estimated using Equation 2 against the values from Norman model simulations. For the of ρ_{cano} estimation, K_ρ of Equation 2 is (b) taken directly on the reference values, (c) determined by the linear regression, and (d) fixed to a constant integer value of 2.0 for all ρ_{leaf}. Note that K_ρ is a coefficient in Equation 2, which is supposed to be adequately determined for the new scheme accuracy.

$\rho_{cano,max}$ increases nearly linearly with larger values of ρ_{leaf}, and the slope of the linear regression is slightly steeper than 1/2 (blue line in Figure 3a). The deviations from the reference values are similar to or less than 5×10^{-5} (Figures 3b and 3c), confirming that the regression line represents reference values accurately.

For a simple representation of the changes in $\rho_{cano,max}$ with respect to ρ_{leaf}, the equation for the regression line was reduced to $y = \frac{1}{2}x$. This indicates that $\rho_{cano,max}$ increases approximately at half the rate of ρ_{leaf}. Although the accuracy reduced by one order of magnitude compared to that of the best-fit regression (Figures 3b and 3c), this simpler equation still yielded quite acceptable results. The deviations from the reference values are at most $\sim 5 \times 10^{-4}$, which is insignificant compared to the changes in the raw values of $\rho_{cano,max}$ according to ρ_{leaf} (Figure 3a).

3.4. Determination of the Parameter K_ρ

The K_ρ in Equation 2, the extinction coefficient, manipulates the shape of the profile of ρ_{cano} values with respect to L. The reference values of K_ρ for different ρ_{leaf} values are obtained by selecting the K_ρ values that best fit the profile of ρ_{cano} calculated by Equation 2 to the Norman model simulations. As a result, 10-values of K_ρ are chosen for 10-ρ_{leaf}-values from 0.01 to 0.10. The reference values of K_ρ are all located near 2.0, and they decrease slightly with an increase in ρ_{leaf} (Figure 4a).

When the reference values of K_ρ are directly substituted into Equation 2, the resultant values of ρ_{cano} appear closely match the Norman model simulations, with deviations of at most $\sim 1 \times 10^{-5}$ (Figure 4b). This indicates that the framework suggested by Equation 2 adequately reproduces the profiles of ρ_{cano} generated from the Norman model simulations.

To achieve a more generalized representation of K_ρ as a function of ρ_{leaf}, two methods are tested to assess the accuracy of the ρ_{cano} determination: (a) K_ρ is represented as a linear regression line along with ρ_{leaf} (solid line in Figure 4a) and (b) K_ρ is kept at a constant integer value of 2 regardless of ρ_{leaf}. With the regression line of K_ρ, the deviation of ρ_{cano} from the Norman model remained under or around 1×10^{-5} (Figure 4c). When using the fixed value of K_ρ, the magnitude of ρ_{cano} deviation increased but less than 1×10^{-4}—i.e., in an acceptable range (Figure 4d).

We proposed two sets of coefficients, considering the trade-off between accuracy and simplicity (Table 3): one for the best-fit coefficients and the other for the simplified coefficients (bottom and middle rows in Table 3, respectively).

3.5. Verification of the New Scheme in Emulating Normal Model

To verify the new schemes, the solutions described in Table 3 were used to calculate ε_{land} and, they were compared with the reference values of the Norman model results (Figure 5). The estimation of the B–L law of

19422466, 2024, 9, Downloaded from https://agupubs.onlinelibrary.wiley.com/doi/10.1029/2023MS003957 by Ewha Womans University Library, Wiley Online Library on [04/03/2025]. See the Terms and Conditions (https://onlinelibrary.wiley.com/terms-and-conditions) on Wiley Online Library for rules of use; OA articles are governed by the applicable Creative Commons License

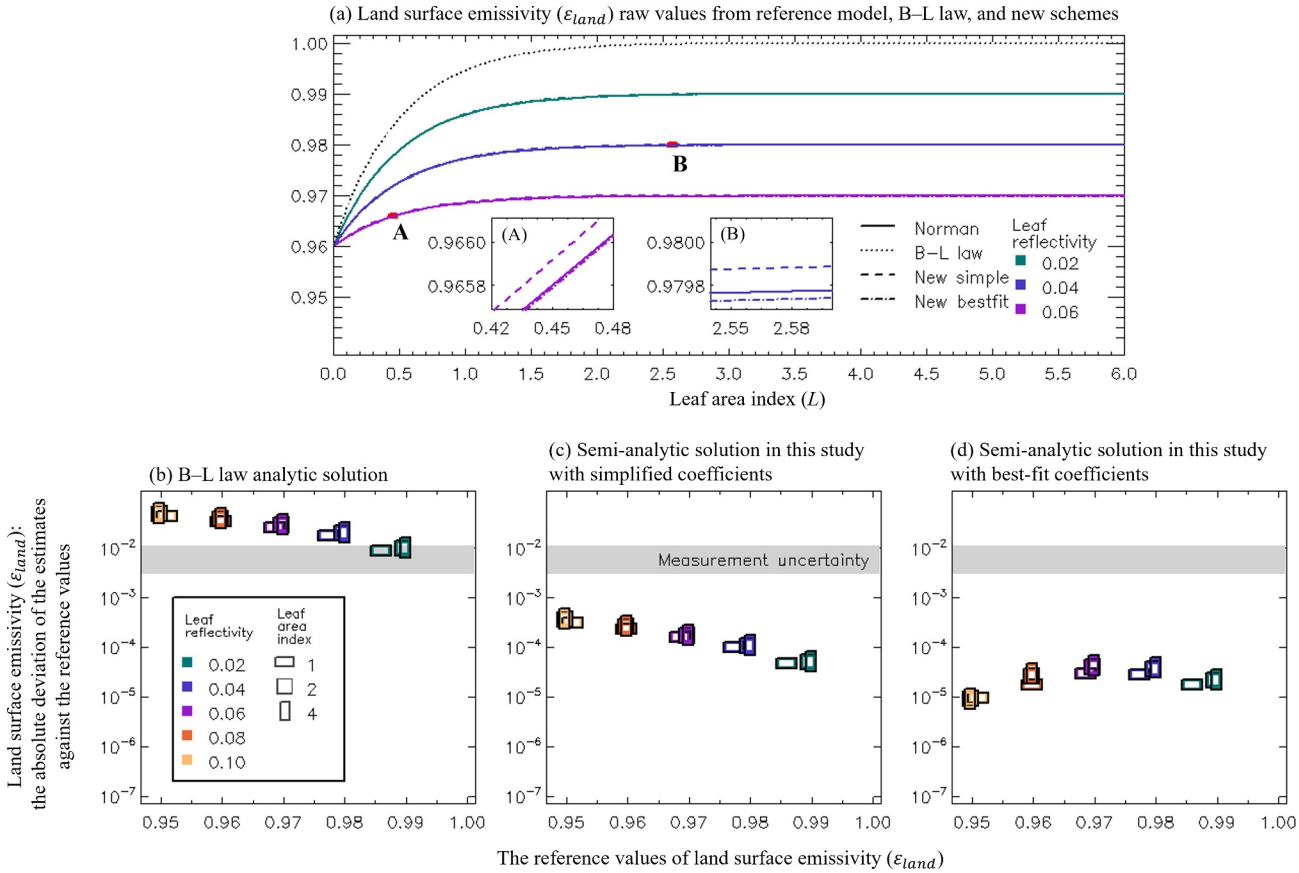


Figure 5. Land surface emissivity (ε_{land}) estimated by a reference model (Norman model), B–L law analytic solution, and two equations sets of the new scheme introduced in Table 3 in this study. (a) The raw values of ε_{land} estimated, and the deviations of ε_{land} against the reference simulations for (b) B–L law analytic solution and the new schemes (semi-analytic solutions) with (c) simplified coefficients and (d) best-fit coefficients. The measurement uncertainties are represented as shaded for the range of 0.003–0.011 with reference to Feltz et al. (2018) and Pérez-Planells et al. (2019). Note that the subplots in (a) are the enlarged views of the sections specified by red boxes titled A and B.

ε_{land} almost reach unity when L is larger than 1, which represents a remarkable overestimation compared to the reference values from the Norman model (black dotted line in Figure 5a) (Note that in Figure 5a, the results from the B–L law are depicted with black lines, not colored, regardless of ρ_{leaf} because the B–L law analytic solution does not consider the value of ρ_{leaf}, and the results from other schemes are depicted with the lines colored depending on the prescribed values of ρ_{leaf}). The deviations of the B–L law against the reference values were shown near and above 1×10^{-2} (Figure 5b). These deviations are greater than the measurement uncertainties (Feltz et al., 2018; Pérez-Planells et al., 2019) and are therefore considered erroneous.

In contrast, the new schemes (i.e., semi-analytic solutions) demonstrates results closely aligned with the reference values. Compared to variations of ε_{land} along with L, the deviations of the new scheme results from the reference values are negligible (Figure 5a, the deviations apparent in sub-plots). The magnitude of the deviations is much smaller in magnitude compared to measurement uncertainties (Figures 5c and 5d). The magnitude of the deviations is at most, 1×10^{-3} for the new scheme with the simplified coefficients (Figure 5c), and this value is further reduced by more than one order of magnitude when using the solution with best-fit coefficients (Figure 5d). Among the two new schemes proposed in Table 3, the simplified solution would be more favored for application to LSMs as it yields practically identical results to the new scheme with the best-fit coefficients.

19422466, 2024, 9, Downloaded from https://agupubs.onlinelibrary.wiley.com/doi/10.1029/2023MS003957 by Ewha Womans University Library, Wiley Online Library on [04/03/2025]. See the Terms and Conditions (https://onlinelibrary.wiley.com/terms-and-conditions) on Wiley Online Library for rules of use; OA articles are governed by the applicable Creative Commons License

19422466, 2024, 9, Downloaded from https://agupubs.onlinelibrary.wiley.com/doi/10.1029/2023MS003957 by Ewha Womans University Library, Wiley Online Library on [04/03/2025]. See the Terms and Conditions (https://onlinelibrary.wiley.com/terms-and-conditions) on Wiley Online Library for rules of use; OA articles are governed by the applicable Creative Commons License

Table 4
A Brief Description of the Numerical Model Experiments Using CLM5

	Calculation of vegetation layer optical properties	Leaf reflectivity (ρ_{leaf})	Adding vegetation layer longwave reflection terms	Reference
CLM-B-L	B–L law analytic solution	0 (assumed in B–L law)	Not matters[a]	Same to CLM5 as released
CLM-NEW	New scheme in Table 3	0.055	Yes	

[a]Yes and No have no difference at all. This is because the B–L law assumes reflectionless of scattering elements in the vegetation layer.

4. Implementation of the New Scheme in CLM5

4.1. The Numerical Experiments With CLM5

The CLM, a global land surface model, has been developed by the National Center for Atmospheric Research (NCAR) over several decades. The most recent release in the CLM series is CLM5, as documented by D. M. Lawrence et al. (2019). As mentioned in the introduction section, CLM series employs the B–L law-based solution to determine the emissivity of the canopy vegetation layer, taking into account the vegetation layer optical depth with L (To elaborate further, CLM considers an additional optical depth due to plant branches and other non-photosynthetic plant parts by the areal fraction index known as stem area index).

The new scheme with simplified coefficients is implemented in CLM5 by modifying the equations for calculating the vegetation optical properties (ε_{cano}, τ_{cano}, ρ_{cano}) using the equations provided in Table 3, thereby replacing the B–L law-based equation. Additionally, a revision is conducted for longwave processes in CLM5 in order to account for terms of radiation flux reflected from the canopy vegetation layer, which were previously omitted. The comprehensive description of the revision in CLM5 to incorporate canopy layer reflection terms can be found in Appendix B. Note that this revision—adding canopy layer reflection terms—does not make any difference when ρ_{leaf} and, consequently, ρ_{cano} is set to zero. This occurs because the new scheme can be reduced to B–L law solution under the condition of zero ρ_{leaf}, resulting in the additional reflection terms having a value of zero. Thus, the implementation of the new scheme allows for the assessment of the effects of leaf reflections with ρ_{leaf} values greater than zero.

In this study, two numerical experiments of CLM5 are conducted, employing the B–L law analytic solution and the new scheme with ρ_{leaf} set to 0.055, respectively, which experiments are referred to as CLM-B-L and CLM-NEW, as described in Table 4. We ran CLM5 historical simulation with satellite phenology, which is recommended by model maintenance community of NCAR as scientifically validated (with the configuration alias of *IHISTClm50Sp*). With this configuration, the globally seasonally varying L is prescribed whose values are consistent with the L data sets retrieved by satellite instruments of the MoDerate Resolution Imaging Spectroradiometer (MODIS) (MCD15A2 v5) averaged for 2001–2015 (P. J. Lawrence & Chase, 2007; D. M. Lawrence et al., 2019). As the standard atmospheric forcing for CLM5 the data set provided by the Global Soil Wetness Project Phase 3 (GSWP3) is utilized, and the forcing data set spans from spans from 1901 to 2014. Because the spin-up period is recommended to be more than 50 simulation-years, the experiments in this study start from 1951 with cold-start until 2014, the last year of the GSWP3 data set. Again, note that the climatology (multi-year average) of monthly MODIS L values is prescribed for each simulation year. The experiment results for the last 14-year from 2001 to 2014 are investigated.

4.2. The Validation of ε_{land} Simulated in CLM5

The values of ε_{land} simulated from CLM5 are validated against satellite-retrieved data set of from CAMEL. The ε_{land} in CLM5 was calculated at each tile (the sub-grids representing land surface heterogeneity) by an equation of $\varepsilon_{land} = 1 - \left(\rho_{cano} + {\tau_{cano}}^2 \times (1 - \varepsilon_{grnd})\right)$, then it is averaged for the grids.

Since the CLM5 experiments in this study employ the L values from the satellite-retrievals of MODIS. Consequently, the ε_{land} calculated in CLM5 corresponds to the MODIS L data set. Because climatology values of L are prescribed, the climatology of ε_{land} are computed by monthly values averaging for the period from 2001 to 2014 for both model simulations and satellite retrievals. The climatology in August for CAMEL

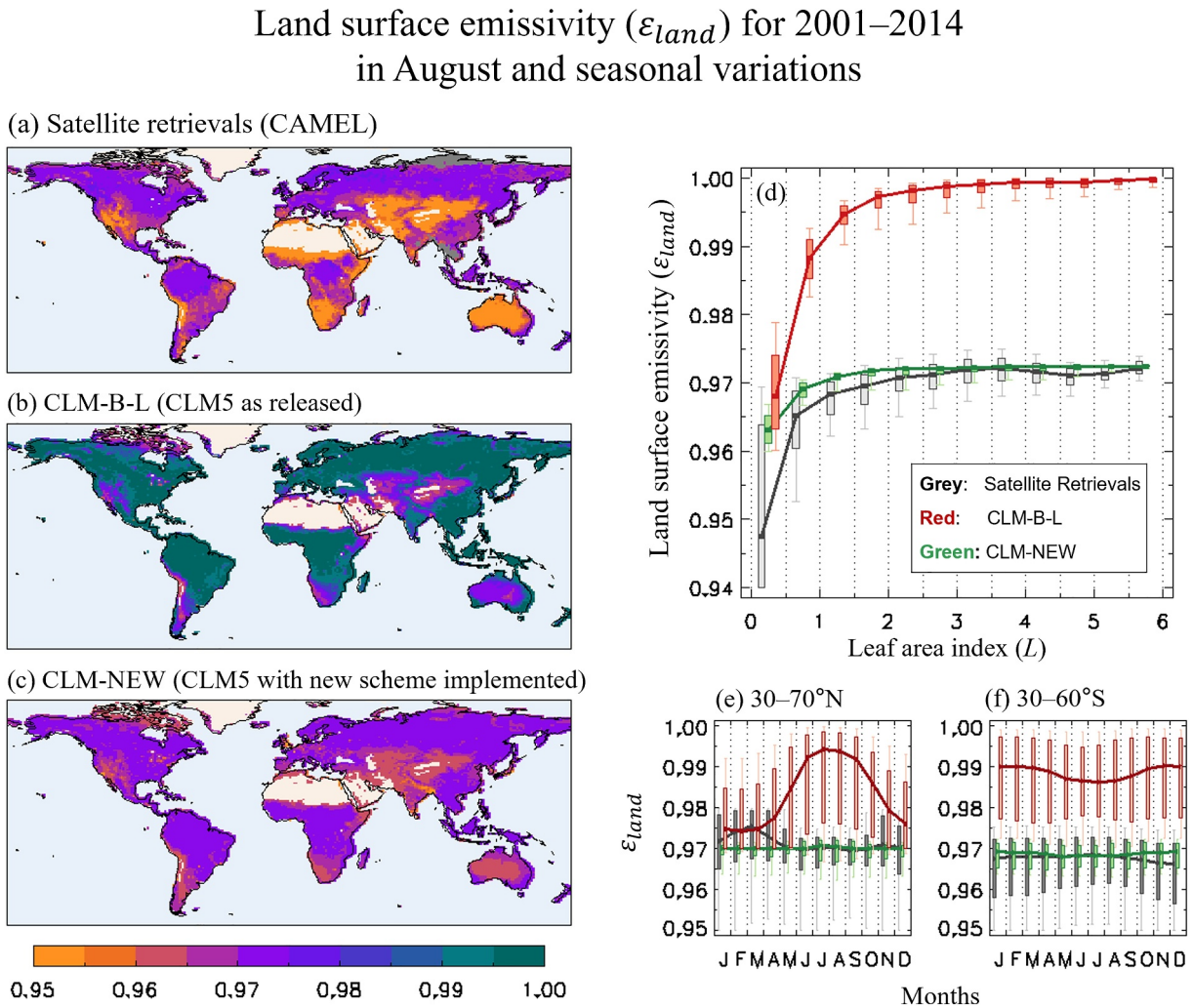


Figure 6. Global distributions of land surface emissivity (ε_{land}) values averaged for the period of 2001–2014. The ε_{land} values in August are shown: (a) retrieved from CAMEL and simulated by CLM5 experiments of (b) CLM-B-L (original CLM5) and (c) CLM-NEW (new scheme implemented CLM5), and (d) distributions with respect to leaf area index (L). The seasonal distributions of ε_{land} are illustrated for regions of (e) 30–70°N and (f) 30–60°S. The box plots in (d)–(f) depicts the distributions of the spatiotemporal ε_{land} values for the bins separated according to (d) L and according to (e) and (f) month. In the box plots, the top and bottom of the of the boxes are the 25th and 75th percentiles, respectively; the bold line in the middle of the boxes is the 50th percentile; the top and bottom whiskers are the 10th and 90th percentiles, respectively.

is illustrated in Figure 6a, and the two-CLM5 experiments are also illustrated in Figures 6b and 6c, respectively.

The simulated ε_{land} in CLM-B-L tends to approach unity in most vegetated regions, leading to an apparent overestimation compared to the satellite retrievals (Figures 6a vs. 6b), as the B–L law solution produces such outcomes (Figure 5a). The ε_{land} increases rapidly with L until it reaches around unity, and the positive bias is apparent also in the sparsely vegetated regions with L values of ~0.5 or larger (see red boxes much higher than gray boxes in Figure 6d). The discrepancy of ε_{land} of CLM-B-L is predominant in the growing season from May to October in the mid and high latitude in the Northern Hemisphere, while the discrepancy is reduced in winter when vegetation layer has a thin optical depth due to leaf fall (Figure 6e). Conversely, the mid latitude regions of the Southern hemisphere mid-latitude consistently exhibit overestimation of ε_{land} through seasons with relatively weak seasonal changes (Figure 6f).

On the other hand, the CLM-NEW experiment, which employs the new scheme, produces ε_{land} with a spatial pattern that closely resembles the satellite retrievals (Figures 6a and 6c). The simulated ε_{land} profile according to L in CLM-NEW aligns well with the satellite-retrievals with deviations less than 0.05 when their medium values are

19422466, 2024, 9, Downloaded from https://agupubs.onlinelibrary.wiley.com/doi/10.1029/2023MS003957 by Ewha Womans University Library, Wiley Online Library on [04/03/2025]. See the Terms and Conditions (https://onlinelibrary.wiley.com/terms-and-conditions) on Wiley Online Library for rules of use; OA articles are governed by the applicable Creative Commons License

19422466, 2024, 9, Downloaded from https://agupubs.onlinelibrary.wiley.com/doi/10.1029/2023MS003957 by Ewha Womans University Library, Wiley Online Library on [04/03/2025]. See the Terms and Conditions (https://onlinelibrary.wiley.com/terms-and-conditions) on Wiley Online Library for rules of use; OA articles are governed by the applicable Creative Commons License

compared, except for very sparsely vegetated regions with $L < 1$, where prescribed values of 0.96 for ε_{grnd} largely determines ε_{land} (Figure 6d). The improved alignment between simulated and observed ε_{land} values remains consistent throughout the seasons for both the Northern and Southern Hemispheres (Figures 6e and 6f). Therefore, it can be concluded that the new scheme enhances the realism of CLM5, particularly concerning surface longwave properties in vegetated regions.

4.3. The Effects of the Enhanced ε_{land} on the Surface Energy Budget in CLM5

The differences of the simulations between the CLM-NEW and CLM-B-L experiments are solely attributed to the effects of longwave leaf reflection, facilitated by the new scheme developed in this study. By prescribing a value of 0.055 to ρ_{leaf} in CLM-NEW, ε_{land} decreases by ~0.03 over densely vegetated regions and seasons. This decrease is particularly evident in mid- and high-latitude Eurasia and Northern America during boreal summer (i.e., June, July, and August) as well as in tropical regions in the central and southern part of Africa and East and Southeast Asia, and a large part of South America throughout all seasons (Figure 6 and the first row of Figure 7). During the dormancy period (i.e., out of the growing season) in the mid- and high-latitude in the Northern Hemisphere, significant differences are shown only in the evergreen forest regions spanning latitudes between 45° and 70°N in Eurasia and North America. On the other hand, arid regions with sparse vegetation, including North Africa, the Middle East, large parts of Central Asia, Tibetan Plateau, and the Andes Mountains, show insignificant effects for all seasons.

In response to the decreased ε_{land}, the upward longwave radiation from the surface ($LW_{\uparrow}$) is also reduced by 1–2 Wm^{-2} for densely vegetated regions (Figure 7, the second row); the spatiotemporal patterns of the $LW_{\uparrow}$ differences correspond to those of ε_{land}. These differences in $LW_{\uparrow}$ persist throughout the investigated period of 2001–2014 without significant interannual and daily variations. The reduction in $LW_{\uparrow}$ is predominantly compensated by an increase in sensible heat flux (Figure 7, third row). On the other hand, the latent heat flux does not exhibit significant changes (Figure 7, fourth raw).

With the changes in the surface fluxes, the skin (radiometric surface) temperature is also changed to increase by up to ~0.2°C for the densely vegetated regions in the tropics (Figure 7, the fifth row). The 2-m temperature shows similar changes to those of skin temperature (figure not shown), but with a much smaller magnitude. This is because the 2-m temperature is partly determined by the prescribed atmospheric forcings in the experiments in this study.

Soil temperatures also increase in most regions and seasons, and their spatiotemporal patterns appear similar to those of the skin temperature but with the following differences: (a) the extent of soil temperature increase appears less than that of skin temperature——the deeper the soil layer, the smaller the temperature differences, as expected, because the heat source is at the land surface; and (b) contrary to the increase in skin temperature, soil temperature decreases, exceptionally, in the high-latitude Northern Hemisphere during the winter season (December, January, and February) for the soil layers within 1.2 m depth from the surface (the top 9 layers in the CLM5; Figure 7, the sixth row).

The decrease of temperature in the near-surface soil layers (1.2 m deep) is mainly due to the reduced snow mass (Figure 7, the bottom row), which weakens the insulation effect and allows more thermal transport from the colder winter atmosphere to the soil layers beneath the surface snow. As a result of the compensation of two contrasting seasonal effects—i.e., near-surface soil layers being colder during snow-covered seasons and warmer during snow-free seasons—deeper soil layers (>1.2 m) show insignificant temperature differences in the high-latitude Northern Hemisphere (Figure 7, the seventh row). Conversely, in tropical regions, the deeper soil layer temperatures show relatively greater differences, where dense vegetation persists throughout all seasons.

5. Summary and Conclusion

Over time, the advancement of LSMs has been driven by the goal of improving their agreement with real-world observations. Particularly in LSMs with higher complexity, which incorporate a radiometric representation of a separated vegetation layer, accurately determining the bulk optical properties of the layer has become a challenging task.

In the context of longwave radiation, the changes in the optical properties of bulk vegetation layer can be derived by a simple analytic solution stemmed from the B–L law. This solution describes the relationship between the leaf

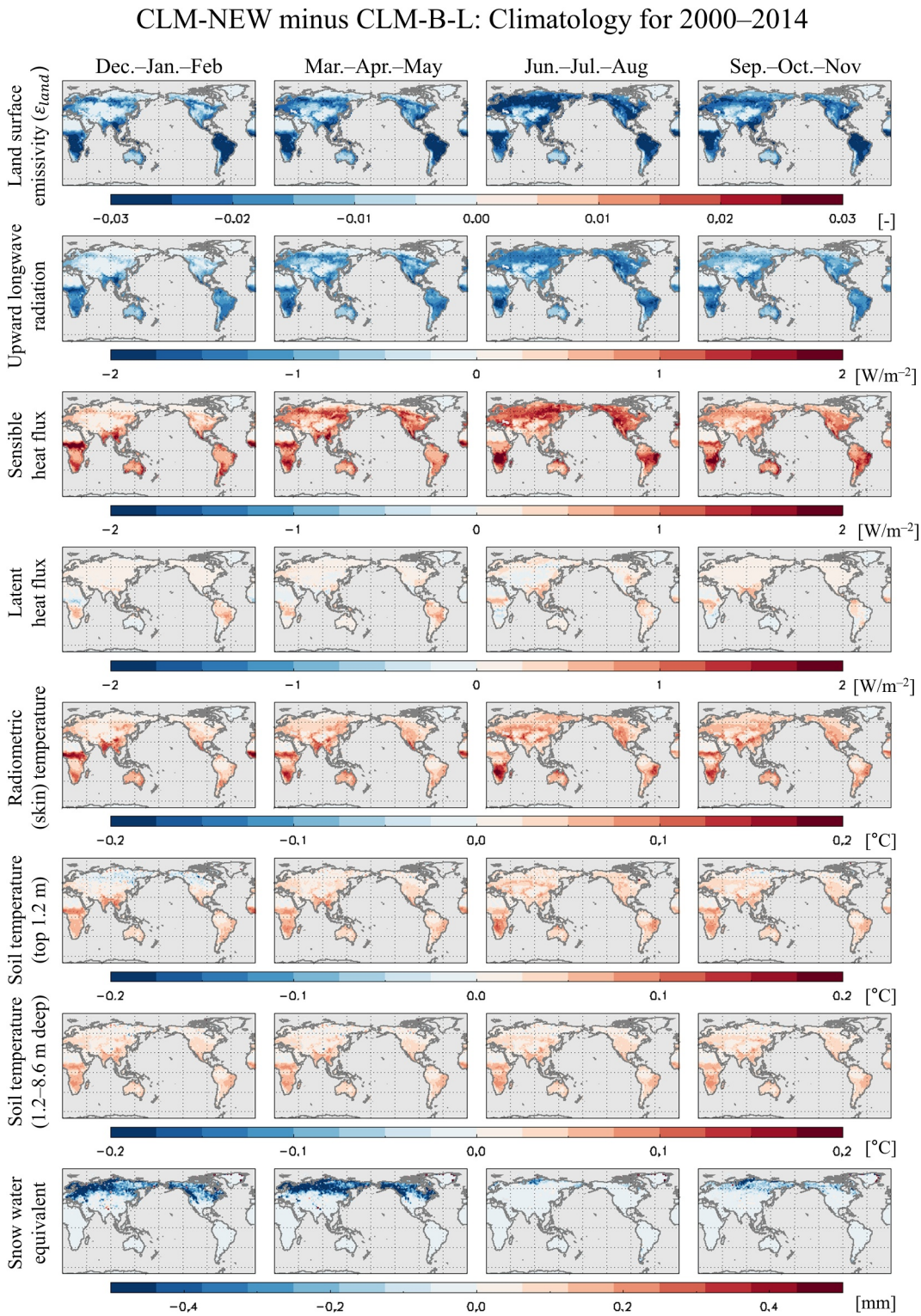


Figure 7. Deviations in land surface emissivity, radiative and turbulent fluxes, land surface skin and soil temperatures, snow water equivalent of the CLM-NEW experiment compared to the CLM-B-L. The illustration presents average values for each season over the period from 2001 to 2014.

19422466, 2024, 9, Downloaded from https://agupubs.onlinelibrary.wiley.com/doi/10.1029/2023MS003957 by Ewha Womans University Library, Wiley Online Library on [04/03/2025]. See the Terms and Conditions (https://onlinelibrary.wiley.com/terms-and-conditions) on Wiley Online Library for rules of use; OA articles are governed by the applicable Creative Commons License

19422466, 2024, 9, Downloaded from https://agupubs.onlinelibrary.wiley.com/doi/10.1029/2023MS003957 by Ewha Womans University Library, Wiley Online Library on [04/03/2025]. See the Terms and Conditions (https://onlinelibrary.wiley.com/terms-and-conditions) on Wiley Online Library for rules of use; OA articles are governed by the applicable Creative Commons License

area index and bulk transmittivity, commonly applied in a few LSMs, including SiB, CLM, and Noah-MP (Other LSMs typically use simpler methods to determine these properties). However, this solution law has a systematic bias, as it tends to overestimate ε_{land}. The B–L law does not consider multiple reflections and assumes zero ρ_{leaf}, leading to zero ρ_{cano}. Consequently, ρ_{cano} appears close to unity when the vegetation layer is optically thick. Therefore, to mitigate the overestimation of ε_{land}, it is essential to consider reflection within canopy vegetation layer.

The new scheme for considering leaf reflections developed in this study consists of a couple of simple equations. Despite its simplicity, it achieves comparable performance to the Norman model, which model involves more computationally costly numerical calculations explicitly addressing multi-reflections among leaves. Upon implementing new scheme in CLM5 with a realistic value of ρ_{leaf}, the simulated ε_{land} becomes much closer to global satellite retrievals, compared to those simulated with the original CLM5 that employs the B–L law solution. The impact of considering leaf reflections on land surface energy budget is evident, with a consistent reduction of 1–2 Wm^{-2} in upward longwave radiation during the vegetation growing season; the reductions are predominantly compensated by an increase in sensible heat flux.

The main benefit of implementing the new scheme is the enhanced realism in land surface longwave optical properties in LSMs, with simulated ε_{land} closely aligning with satellite retrieval values for vegetated regions. The ε_{land} values simulated in CLM5 remain within the ranges of the satellite retrievals for pre-growing seasons regardless of the new scheme implementation (Figure 6e). This stems from the fact that soil surface emissivity and snow surface emissivity parameters dominantly determine the ε_{land} value in the pre-growing season, and these parameters are prescribed with observation-representative values of 0.96 and 0.97, respectively. However, during the growing season when land surface is covered by leaves, the original CLM5 exhibits a significant discrepancy from the observations due to the systematic bias of the B–L law solution. This gap is largely closed by considering leaf reflectivity through the implemented new scheme.

Model experiments, in this study, are confined to offline LSM experiments. However, in an atmosphere–land coupled model, the effects of considering realistic leaf reflections identified in the offline experiments can be amplified by interactions with atmospheric components, at least regionally. For instance, Jin and Liang (2006) exhibited that the modifications of land surface emissivity has a more pronounced impact in the atmosphere–land coupled model than the land offline model in the target regions.

With offline LSM experiments, the consideration of realistic leaf reflections led to changes in land surface energy partitioning: a decrease in upward longwave flux and a corresponding increase in sensible heat flux over a large portion of vegetated lands during summer, both by 1–2 Wm^{-2}. This altered partitioning could influence the atmospheric temperatures differently depending on its altitude, because sensible heat is more likely to be sequestered by the lower atmosphere than upward longwave radiation. Possibly, the altered partitioning leads to a warmer planetary boundary layer and a cooler free atmosphere with a significant presence of water vapor or other longwave-absorbing elements. These changes in atmospheric temperature profiles can alter cloud formation conditions, thereby providing feedback to land surface through modifications in solar radiation. Given the variability of cloud formation in response to surface heat flux across regions and seasons (Findell & Eltahir, 2003a, 2003b), further comprehensive assessments of land–atmosphere interactions are required, particularly utilizing land–atmosphere coupled climate or weather models.

Despite the advancements made by new scheme, resulting in realistic simulations of land surface emissivity, there is still room for further development of the scheme, especially in regions with sparsely vegetated (e.g., $L < 1$). The current new scheme assumes horizontally oriented and randomly distributed leaves, corresponding to unity value of the extinction coefficient of K_d in Equation A5. Realistic K_d values rather than unity, representing actual leaf inclinations and clumpings, would alters the ε_{land} profile along with L, while keeping ε_{land} values unchanged at zero-L and asymptote, enabling adjustment of ε_{land} values for sparsely vegetated regions. Additionally, these sparsely vegetated zones are influenced by both soil-exposed and leaf-covered surfaces, necessitating more comprehensive approaches for further study.

19422466, 2024, 9, Downloaded from https://agupubs.onlinelibrary.wiley.com/doi/10.1029/2023MS003957 by Ewha Womans University Library, Wiley Online Library on [04/03/2025]. See the Terms and Conditions (https://onlinelibrary.wiley.com/terms-and-conditions) on Wiley Online Library for rules of use; OA articles are governed by the applicable Creative Commons License

Appendix A: Basis Theory of Canopy Layer Radiative Transfer

A1. The Pre-Existing Methods

a. Norman model

In the case of vegetation layers in which horizontal scale is significantly larger than the scale of individual plants and the spaces between them, as commonly seen in most LSMs, it is adequately acceptable to decompose the radiative beams traversing a vegetation layer into following two components: the radiant upward and downward (or sky-ward and ground-ward) fluxes. Additionally, when the plant canopy is assumed to comprise only leaves and empty space, the radiometric processes on a canopy layer characterized by three components: (a) the interception of the radiation by leaves scattering forward through the leaf medium; (b) the interception of the radiation by leaves scattering backward; and (c) the transmission of the radiation passing through the empty (or leaf-absent) part of the canopy layer. With this framework, a canopy radiative transfer model was introduced by Norman (1979) as follows:

$$I_i^{\downarrow} = I_{i+1}^{\downarrow}[\tau_d + (1-\tau_d)\tau_{leaf}] + I_i^{\uparrow}\rho_{leaf}(1-\tau_d) \tag{A1}$$

$$I_{i+1}^{\uparrow} = I_i^{\uparrow}[\tau_d + (1-\tau_d)\tau_{leaf}] + I_{i+1}^{\downarrow}\rho_{leaf}(1-\tau_d) \tag{A2}$$

where $I_i^{\downarrow}$ is the downward flux below layer $i+1$ onto layer i and, likewise, $I_i^{\uparrow}$ is the upward flux above layer i onto layer $i+1$, and τ_d indicates the ratio of the irradiance transmitted through a layer without any interception by leaves to the entire radiation incident onto the layer, which is calculated as $\tau_d = \exp(-K_d L_i)$, where K_d is the extinction coefficient or the optical depth per L of diffused radiation, L_i is the L value of layer i, and τ_{leaf} is the leaf transmittivity.

To solve these equations, an iterative numerical method proposed by Norman (1979) can be employed. For the N-layers, the left-side terms of Equations A1 and A2 are computed using initial estimates of the upward and downward fluxes on both sides of the entire layers. Following this, the computed results of the left side of Equations A1 and A2 are repeatedly substituted to the right-hand side of the same equations until the resultant fluxes converge and do not change significantly. An alternative numerical solution involves utilizing the tri-diagonal system of equations reformed from Equations A1 and A2, which is employed in this study. The details on these numerical methods are referred to Bonan (2019).

b. The linkage of the B–L law-based analytic solution to the Norman model

Exactly, the B–L law-based analytic solution can be derived from Equation A1 when ρ_{leaf} is assumed to be zero. By imposing this assumption, the second term on the right-hand side of Equation A1 can be eliminated. When L is small, $\tau_d = 1 - K_d L$, and Equation A1 can be rewritten as follows:

$$I_{i+1}^{\downarrow}/I_i^{\downarrow} = 1 - \varepsilon_{leaf} K_d L_i \tag{A3}$$

where ε_{leaf} is the leaf emissivity. For N layers with identical L_i of ΔL ($\Delta L = L/N$), τ_{cano} can be calculated as follows:

$$\tau_{cano} = (1 - \varepsilon_{leaf} K_d \Delta L)^{L/\Delta L} \tag{A4}$$

For small ΔL, Equation A4 can be rewritten using L'Hospital's rule as follows:

$$\tau_{cano} = \exp(-\varepsilon_{leaf} K_d L) \tag{A5}$$

This equation can be reduced under the assumption of the radiometrically black leaf (ε_{leaf} is unity) and horizontal and randomly distributed leaves (K_d is unity), as follows:

$$\varepsilon_{cano} = 1 - \exp(-L) \tag{A6}$$

19422466, 2024, 9, Downloaded from https://agupubs.onlinelibrary.wiley.com/doi/10.1029/2023MS003957 by Ewha Womans University Library, Wiley Online Library on [04/03/2025]. See the Terms and Conditions (https://onlinelibrary.wiley.com/terms-and-conditions) on Wiley Online Library for rules of use; OA articles are governed by the applicable Creative Commons License

where the unity parameter of K_d in Equation A5 is omitted.

Equation A6 was initially derived by Monsi (1953) utilizing its corresponding vertical profiles of radiative measurements in forests. Subsequently, this equation was initially implemented in an LSM called the Simple Biosphere Model (SiB; Sellers et al., 1986) to calculate the longwave energy budget of the canopy bulk layer. This approach has been inherited by a few LSMs, including the CLM and Noah-MP. It is noteworthy that the CLM employs Equation A6 including the parameter of the average inverse optical depth (μ)—which is the inverse of K_d, and it is also prescribed as unity—expressed as follows: $\varepsilon_{cano} = 1 - \exp(-L/\mu)$.

Appendix B: Application of the New Method to CLM5

B1. Revising CLM5 for Considering Vegetation Layer Reflection

In original CLM5, the terms for longwave reflection onto the canopy vegetation layer are omitted in the calculations of the surface energy balance. This is because the vegetation layer is assumed to be non-reflective, following the assumption of B–L law of no reflective leaves in the original CLM5. The implementation of the new scheme into CLM5 frees it from the constraint imposed by this assumption, necessitating consideration of reflection terms.

The terms for vegetation layer reflection are incorporated into the longwave process calculations in CLM5. Three equations governing longwave flux are augmented: the upward longwave radiation above the vegetation layer ($LW_{atm\uparrow}$), net longwave radiation flux for ground ($\overrightarrow{LW}_{grnd}$), and net longwave radiation flux for canopy layer ($\overrightarrow{LW}_{cano}$). To represent the terms related to multi-reflection simply, the factors for multi-reflections are introduced as follows:

$$m_{2cg} = \left[1 + \rho_{cano}(1 - \varepsilon_{grnd})\left[\left(1 + \rho_{cano}(1 - \varepsilon_{grnd})\right)\right]\right]$$

$$m_{3cg} = \left[1 + \rho_{cano}(1 - \varepsilon_{grnd})\left[1 + \rho_{cano}(1 - \varepsilon_{grnd})\left[1 + \rho_{cano}(1 - \varepsilon_{grnd})\right]\right]\right]$$

19422466, 2024, 9, Downloaded from https://agupubs.onlinelibrary.wiley.com/doi/10.1029/2023MS003957 by Ewha Womans University Library, Wiley Online Library on [04/03/2025]. See the Terms and Conditions (https://onlinelibrary.wiley.com/terms-and-conditions) on Wiley Online Library for rules of use; OA articles are governed by the applicable Creative Commons License

Table B1
Longwave Flux Equations in the Vegetated Land Surface in CLM5

Upward longwave radiation above vegetation, $LW_{\uparrow}$

In the original CLM5:

$$LW_{\uparrow} = {\tau_{cano}}^2(1-\varepsilon_{grnd})\cdot LW_{atm\downarrow} + \varepsilon_{cano}(1+\tau_{cano}(1-\varepsilon_{grnd}))\cdot\sigma T_{cano}^4 + \varepsilon_{grnd}\tau_{cano}\cdot\sigma T_{grnd}^4$$

This expression can be expanded with individual terms as:

$$LW_{\uparrow} = aa_2\cdot LW_{atm\downarrow} + (va_1+va_2)\cdot\sigma T_{cano}^4 + ga_1\cdot\sigma T_{grnd}^4$$

In the revised CLM5:

$$LW_{\uparrow} = \left(\rho_{cano}+{\tau_{cano}}^2(1-\varepsilon_{grnd})\cdot M_{2cg}\right)\cdot LW_{atm\downarrow} + \varepsilon_{cano}(1+\tau_{cano}(1-\varepsilon_{grnd})\cdot M_{2cg})\cdot\sigma T_{cano}^4 + \varepsilon_{grnd}\tau_{cano}\cdot M_{2cg}\cdot\sigma T_{grnd}^4$$

This expression can be expanded with individual terms as:

$$LW_{\uparrow} = (aa_1+aa_2+aa_3+aa_4)\cdot LW_{atm\downarrow} + (va_1+va_2+va_3+va_4)\cdot\sigma T_{cano}^4 + \left(ga_1+ga_2+ga_3\right)\cdot\ \sigma T_{grnd}^4$$

Net longwave radiation flux for ground, $\overrightarrow{LW}_{grnd}$

In the original CLM5:

$$\overrightarrow{LW}_{grnd} = \tau_{cano}\varepsilon_{grnd}\cdot LW_{atm\downarrow} + \varepsilon_{cano}\varepsilon_{grnd}\cdot\sigma T_{cano}^4 - \varepsilon_{grnd}\cdot\sigma T_{grnd}^4$$

This expression can be expanded with individual terms as:

$$\overrightarrow{LW}_{grnd} = ag_1\cdot LW_{atm\downarrow} + vg_1\cdot\sigma T_{cano}^4 - \varepsilon_{grnd}\cdot\sigma T_{grnd}^4$$

In the revised CLM5:

$$\overrightarrow{LW}_{grnd} = \tau_{cano}\varepsilon_{grnd}M_{2cg}\cdot LW_{atm\downarrow} + \varepsilon_{cano}\varepsilon_{grnd}M_{3cg}\cdot\sigma T_{cano}^4 + \varepsilon_{grnd}\left(\varepsilon_{grnd}\rho_{cano}M_{3cg}-1\right)\cdot\sigma T_{grnd}^4$$

This expression can be expanded with individual terms as:

$$\overrightarrow{LW}_{grnd} = \left(ag_1+ag_2+ag_3\right)\cdot LW_{atm\downarrow} + \left(vg_1+vg_2+vg_3+vg_4\right)\cdot\sigma T_{cano}^4 + \left(gg_1+gg_2+gg_3+gg_4-\varepsilon_{grnd}\right)\cdot\sigma T_{grnd}^4$$

Net longwave radiation flux for canopy layer, $\overrightarrow{LW}_{cano}$

In the original CLM5:

$$\overrightarrow{LW}_{cano} = \varepsilon_{cano}(1+\tau_{cano}(1-\varepsilon_{grnd}))\cdot LW_{atm\downarrow} + \varepsilon_{cano}(\varepsilon_{cano}(1-\varepsilon_{grnd})-2)\cdot\sigma T_{cano}^4 + \varepsilon_{grnd}\varepsilon_{cano}\cdot\sigma T_{grnd}^4$$

This expression can be expanded with individual terms as:

$$\overrightarrow{LW}_{cano} = (av_1+av_2)\cdot LW_{atm\downarrow} + (vv_1-2\varepsilon_{cano})\cdot\sigma T_{cano}^4 + gv_1\ \cdot\sigma T_{grnd}^4$$

In the revised CLM5:

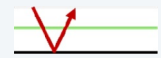
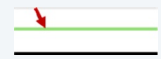
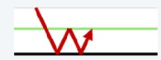
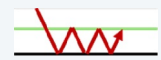
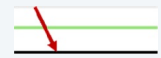
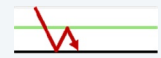
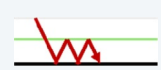
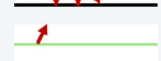
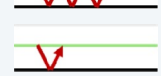
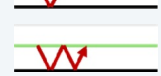
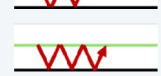
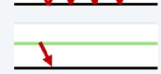
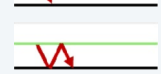
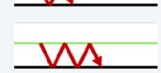
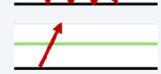
$$\overrightarrow{LW}_{cano} = \varepsilon_{cano}(1+\tau_{cano}(1-\varepsilon_{grnd}))M_{2cg}\cdot LW_{atm\downarrow} + \varepsilon_{cano}((1-\varepsilon_{grnd})\varepsilon_{cano}M_{3cg}-2)\cdot\sigma T_{cano}^4 + \varepsilon_{grnd}\varepsilon_{cano}M_{3cg}\cdot\sigma T_{grnd}^4$$

This expression can be expanded with individual terms as:

$$\overrightarrow{LW}_{cano} = (av_1+av_2+av_3+av_4)\cdot LW_{atm\downarrow} + (vv_1+vv_2+vv_3+vv_4-2\varepsilon_{cano})\cdot\sigma T_{cano}^4 + \left(gv_1+gv_2+gv_3+gv_4\right)\ \cdot\sigma T_{grnd}^4$$

Note. The original and revised equations for longwave fluxes are compared with its expanded forms consisting of individual longwave terms.

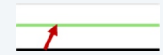
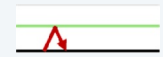
Table B2
Individual Terms of Longwave Fluxes in the Vegetated Land Surface of CLM5, Along With Corresponding Schematics

Longwave flux terms	Schematics	Order[a]
$aa_1 = \rho_{cano}$		−1
$\boldsymbol{aa_2 = \tau_{cano}{}^2(1-\varepsilon_{grnd})}$		−1
$aa_3 = \tau_{cano}{}^2(1-\varepsilon_{grnd})^2\rho_{cano}$		−4
$aa_4 = \tau_{cano}{}^2(1-\varepsilon_{grnd})^3\rho_{cano}{}^2$		−8
$\boldsymbol{av_1 = \varepsilon_{cano}}$		0
$\boldsymbol{av_2 = \varepsilon_{cano}\tau_{cano}(1-\varepsilon_{grnd})}$		−2
$av_3 = \varepsilon_{cano}\tau_{cano}(1-\varepsilon_{grnd})^2\rho_{cano}$		−6
$av_4 = \varepsilon_{cano}\tau_{cano}(1-\varepsilon_{grnd})^3\rho_{cano}{}^2$		−9
$\boldsymbol{ag_1 = \tau_{cano}\varepsilon_{grnd}}$		0
$ag_2 = \tau_{cano}\varepsilon_{grnd}\rho_{cano}(1-\varepsilon_{grnd})$		−3
$ag_3 = \tau_{cano}\varepsilon_{grnd}\rho_{cano}{}^2(1-\varepsilon_{grnd})^2$		−7
$\boldsymbol{va_1 = \varepsilon_{cano}}$		0
$\boldsymbol{va_2 = \varepsilon_{cano}\tau_{cano}(1-\varepsilon_{grnd})}$		−2
$va_3 = \varepsilon_{cano}\tau_{cano}(1-\varepsilon_{grnd})^2\rho_{cano}$		−6
$va_4 = \varepsilon_{cano}\tau_{cano}(1-\varepsilon_{grnd})^3\rho_{cano}{}^2$		−9
$\boldsymbol{vv_1 = \varepsilon_{cano}{}^2(1-\varepsilon_{grnd})}$		−1
$vv_2 = \varepsilon_{cano}{}^2(1-\varepsilon_{grnd})^2\rho_{cano}$		−3
$vv_3 = \varepsilon_{cano}{}^2(1-\varepsilon_{grnd})^3\rho_{cano}{}^2$		−6
$vv_4 = \varepsilon_{cano}{}^2(1-\varepsilon_{grnd})^4\rho_{cano}{}^3$		−9
$\boldsymbol{vg_1 = \varepsilon_{cano}\varepsilon_{grnd}}$		0
$vg_2 = \varepsilon_{cano}\varepsilon_{grnd}\rho_{cano}(1-\varepsilon_{grnd})$		−2
$vg_3 = \varepsilon_{cano}\varepsilon_{grnd}\rho_{cano}{}^2(1-\varepsilon_{grnd})^2$		−5
$vg_4 = \varepsilon_{cano}\varepsilon_{grnd}\rho_{cano}{}^3(1-\varepsilon_{grnd})^3$		−7
$\boldsymbol{ga_1 = \varepsilon_{grnd}\tau_{cano}}$		0
$ga_2 = \varepsilon_{grnd}\tau_{cano}\rho_{cano}(1-\varepsilon_{grnd})$		−3

19422466, 2024, 9, Downloaded from https://agupubs.onlinelibrary.wiley.com/doi/10.1029/2023MS003957 by Ewha Womans University Library, Wiley Online Library on [04/03/2025]. See the Terms and Conditions (https://onlinelibrary.wiley.com/terms-and-conditions) on Wiley Online Library for rules of use; OA articles are governed by the applicable Creative Commons License

19422466, 2024, 9, Downloaded from https://agupubs.onlinelibrary.wiley.com/doi/10.1029/2023MS003957 by Ewha Womans University Library, Wiley Online Library on [04/03/2025]. See the Terms and Conditions (https://onlinelibrary.wiley.com/terms-and-conditions) on Wiley Online Library for rules of use; OA articles are governed by the applicable Creative Commons License

Table B2
Continued

Longwave flux terms	Schematics	Order[a]
$ga_3 = \varepsilon_{grnd}\tau_{cano}{\rho_{cano}}^2(1-\varepsilon_{grnd})^2$		−7
$\boldsymbol{gv_1 = \varepsilon_{grnd}\varepsilon_{cano}}$		0
$gv_2 = \varepsilon_{grnd}\varepsilon_{cano}\rho_{cano}(1-\varepsilon_{grnd})$		−2
$gv_3 = \varepsilon_{grnd}\varepsilon_{cano}{\rho_{cano}}^2(1-\varepsilon_{grnd})^2$		−5
$gv_4 = \varepsilon_{grnd}\varepsilon_{cano}{\rho_{cano}}^3(1-\varepsilon_{grnd})^3$		−7
$gg_1 = {\varepsilon_{grnd}}^2\rho_{cano}$		−1
$gg_2 = {\varepsilon_{grnd}}^2{\rho_{cano}}^2(1-\varepsilon_{grnd})$		−3
$gg_3 = {\varepsilon_{grnd}}^2{\rho_{cano}}^3(1-\varepsilon_{grnd})^2$		−6
$gg_4 = {\varepsilon_{grnd}}^2{\rho_{cano}}^4(1-\varepsilon_{grnd})^3$		−9

Note. The longwave terms with an order equal to or greater than –9 is listed and utilized for the CLM-NEW experiment. The terms used for the original CLM5 and the CLM-B-L experiment are highlighted in bold. [a]The order is calculated by CEIL ($\log_{10}x$), where CEIL() is the ceiling function for rounding off real values.

Here, m_{2cg} and m_{3cg} indicates the additional weight gained from two-times and three-times reflections between canopy vegetation layer and ground surface, respectively. The augmented equations of longwave fluxes in CLM5 are organized in Table B1. Note that among the radiation terms considering vegetation layer reflections, only numerically practical terms are included in the augmentation of the flux equations. Specifically, the terms with an order equal to or greater than −9 (raw value than 10^{-9}) are chosen. For the assessments of the orders of terms, the practical range of L simulated in CLM5, ranging from 0.05 to 7, is considered with the ρ_{leaf} value of 0.1. The selected terms are detailed in Table B2.

Data Availability Statement

Satellite data sets used in this study are all provided from the Land Processes Distributed Active Archive Center (LP DAAC). Specifically, the satellite retrieval data set of land surface emissivity of the CAMEL is accessible at https://lpdaac.usgs.gov/products/cam5k30emv002 (Hook, 2017), the satellite retrievals of land surface temperatures of the MOD11C3 is accessible at https://lpdaac.usgs.gov/products/mod11c3v061 (Wan et al., 2021). The CLM5 is freely available at https://escomp.github.io/ctsm-docs/versions/release-clm5.0/html (D. Lawrence et al., 2018). The source codes written for all analysis in this study are available at https://zenodo.org/records/10617596 (Gim & Park, 2023).

Acknowledgments
We thank the four anonymous reviewers for their constructive comments and suggestions. This work was carried out through the R&D project "Development of the Next-Generation Numerical Weather Prediction Model of the Korea Institute of Atmospheric Prediction Systems (KIAPS)," funded by the Korea Meteorological Administration (KMA2020-02212). It is partly supported by the National Research Foundation of Korea (NRF) grant funded by the Korea government (MSIT) (NRF-2021R1A2C1095535) and under the grant of Basic Science Research Program through the NRF funded by the Ministry of Education (2018R1A6A1A08025520). We are grateful to NCAR for its open-source policy and for allowing us to use CLM5 model.

References

Arp, G. K., & Phinney, D. E. (1980). Ecological variations in thermal infrared emissivity of vegetation. *Environmental and Experimental Botany*, *20*(2), 135–148. https://doi.org/10.1016/0098-8472(80)90006-4

Baldocchi, D. D., & Harley, P. C. (1995). Scaling carbon dioxide and water vapour exchange from leaf to canopy in a deciduous forest. II. Model testing and application. *Plant, Cell and Environment*, *18*(10), 1157–1173. https://doi.org/10.1111/j.1365-3040.1995.tb00626.x

Baret, F., Morissette, J., Fernandes, R., Champeaux, J., Myneni, R., Chen, J., et al. (2006). Evaluation of the representativeness of networks of sites for the global validation and intercomparison of land biophysical products: Proposition of the CEOS-BELMANIP. *IEEE Transactions on Geoscience and Remote Sensing*, *44*(7), 1794–1803. https://doi.org/10.1109/tgrs.2006.876030

Best, M. J., Pryor, M., Clark, D. B., Rooney, G. G., Essery, R. L. H., Ménard, C. B., et al. (2011). The Joint UK Land Environment Simulator (JULES), model description—Part 1: Energy and water fluxes. *Geoscientific Model Development*, *4*(3), 677–699. https://doi.org/10.5194/gmd-4-677-2011

Bonan, G. (2019). *Climate change and terrestrial ecosystem modeling*. Cambridge University Press.

Borbas, E. E., Hulley, G., Feltz, M., Knuteson, R., & Hook, S. (2018). The combined ASTER MODIS emissivity over land (CAMEL) Part 1: Methodology and high spectral resolution application. *Remote Sensing*, *10*(4), 643. https://doi.org/10.3390/rs10040643

Chalmers, J. (2013). Infrared spectroscopy| sample presentation. In *Reference module in chemistry, molecular sciences and chemical engineering*. Elsevier.

Cheng, J., Liang, S., Yao, Y., & Zhang, X. (2013). Estimating the optimal broadband emissivity spectral range for calculating surface longwave net radiation. *IEEE Geoscience and Remote Sensing Letters*, *10*(2), 401–405. https://doi.org/10.1109/lgrs.2012.2206367

Dickinson, R. E., Shaikh, M., Bryant, R., & Graumlich, L. (1998). Interactive canopies for a climate model. *Journal of Climate*, *11*(11), 2823–2836. https://doi.org/10.1175/1520-0442(1998)011<2823:icfacm>2.0.co;2

Ek, M. B., Mitchell, K. E., Lin, Y., Rogers, E., Grunmann, P., Koren, V., et al. (2003). Implementation of Noah land surface model advances in the National Centers for Environmental Prediction operational mesoscale Eta model. *Journal of Geophysical Research*, *108*(D22), 8851. https://doi.org/10.1029/2002jd003296

Feltz, M., Borbas, E., Knuteson, R., Hulley, G., & Hook, S. (2018). The combined ASTER and MODIS emissivity over land (CAMEL) global broadband infrared emissivity product. *Remote Sensing*, *10*(7), 1027. https://doi.org/10.3390/rs10071027

Findell, K. L., & Eltahir, E. A. B. (2003a). Atmospheric controls on soil moisture–boundary layer interactions. Part I: Framework development. *Journal of Hydrometeorology*, *4*(3), 552–569. https://doi.org/10.1175/1525-7541(2003)004<0552:acosml>2.0.co;2

Findell, K. L., & Eltahir, E. A. B. (2003b). Atmospheric controls on soil moisture–boundary layer interactions. Part II: Feedbacks within the Continental United States. *Journal of Hydrometeorology*, *4*(3), 570–583. https://doi.org/10.1175/1525-7541(2003)004<0570:acosml>2.0.co;2

Fisher, R. A., & Koven, C. D. (2020). Perspectives on the future of land surface models and the challenges of representing complex terrestrial systems. *Journal of Advances in Modeling Earth Systems*, *12*(4), e2018MS001453. https://doi.org/10.1029/2018ms001453

Francois, C., Ottle, C., & Prevot, L. (1997). Analytical parameterization of canopy directional emissivity and directional radiance in the thermal infrared. Application on the retrieval of soil and foliage temperatures using two directional measurements. *International Journal of Remote Sensing*, *18*(12), 2587–2621. https://doi.org/10.1080/014311697217495

Gim, H. J., & Park, S. K. (2023). Code and Data: Analytic parameterization of longwave optical properties of bulk vegetation layer permitting non-zero leaf reflectivity for land surface model applications [Software]. *Zenodo*. https://zenodo.org/records/10617596

Hook, S. (2017). Combined ASTER and MODIS emissivity database over land (CAMEL) emissivity monthly global 0.05Deg V002 [Dataset]. *NASA EOSDIS Land Processes Distributed Active Archive Center*. https://doi.org/10.5067/MEaSUREs/LSTE/CAM5K30EM.002

Jin, M., Dickinson, R. E., & Vogelmann, A. M. (1997). A comparison of CCM2–BATS skin temperature and surface-air temperature with satellite and surface observations. *Journal of Climate*, *10*(7), 1505–1524. https://doi.org/10.1175/1520-0442(1997)010<1505:acocbs>2.0.co;2

Jin, M., & Liang, S. (2006). An improved land surface emissivity parameter for land surface models using global remote sensing observations. *Journal of Climate*, *19*(12), 2867–2881. https://doi.org/10.1175/jcli3720.1

Krinner, G., Viovy, N., de Noblet-Ducoudré, N., Ogée, J., Polcher, J., Friedlingstein, P., et al. (2005). A dynamic global vegetation model for studies of the coupled atmosphere-biosphere system. *Global Biogeochemical Cycles*, *19*(1). https://doi.org/10.1029/2003gb002199

Lawrence, D., Fisher, R., Koven, C., Oleson, K., Swenson, S., & Vertenstein, M. (2018). Technical description of version 5.0 of the community land model (CLM) [Software]. https://escomp.github.io/ctsm-docs/versions/release-clm5.0/html/

Lawrence, D. M., Fisher, R. A., Koven, C. D., Oleson, K. W., Swenson, S. C., Bonan, G., et al. (2019). The community land model version 5: Description of new features, benchmarking, and impact of forcing uncertainty. *Journal of Advances in Modeling Earth Systems*, *11*(12), 4245–4287. https://doi.org/10.1029/2018ms001583

Lawrence, P. J., & Chase, T. N. (2007). Representing a new MODIS consistent land surface in the Community Land Model (CLM 3.0). *Journal of Geophysical Research*, *112*(G1), G01023. https://doi.org/10.1029/2006jg000168

Loveless, M., Borbas, E. E., Knuteson, R., Cawse-Nicholson, K., Hulley, G., & Hook, S. (2021). Climatology of the combined ASTER MODIS emissivity over land (CAMEL) version 2. *Remote Sensing*, *13*(1), 111. https://doi.org/10.3390/rs13010111

Luo, J., Huang, A., Lyu, S., Lin, Z., Gu, C., Li, Z., et al. (2023). Improved performance of CLM5.0 model in frozen soil simulation over Tibetan Plateau by implementing the vegetation emissivity and gravel hydrothermal schemes. *Journal of Geophysical Research: Atmospheres*, *128*(6), e2022JD038021. https://doi.org/10.1029/2022jd038021

Ma, X., Jin, J., Liu, J., & Niu, G.-Y. (2019). An improved vegetation emissivity scheme for land surface modeling and its impact on snow cover simulations. *Climate Dynamics*, *53*(9), 6215–6226. https://doi.org/10.1007/s00382-019-04924-9

Manabe, S. (1969). Climate and the ocean circulation: I. The atmospheric circulation and the hydrology of the Earth's surface. *Monthly Weather Review*, *97*(11), 739–774. https://doi.org/10.1175/1520-0493(1969)097<0739:catoc>2.3.co;2

Monsi, M. (1953). Uber den Lichtfaktor in den Pflanzen-gesellschaften und seine Bedeutung fur die Stoffproduktion. *Japanese Journal of Botany*, *14*, 22–52.

Niu, G.-Y., Yang, Z. L., Mitchell, K. E., Chen, F., Ek, M. B., Barlage, M., et al. (2011). The community Noah land surface model with multi-parameterization options (Noah-MP): 1. Model description and evaluation with local-scale measurements. *Journal of Geophysical Research*, *116*(D12), D12109. https://doi.org/10.1029/2010jd015139

Norman, J. (1979). Modeling the complete crop canopy. In G. Barfield, (Ed.), *Modification of the aerial environment of crops* (Vol. 249, p. 280). American Society of Agricultural Engineers.

Pérez-Planells, L., Valor, E., Niclòs, R., Coll, C., Puchades, J., & Campos-Taberner, M. (2019). Evaluation of six directional canopy emissivity models in the thermal infrared using emissivity measurements. *Remote Sensing*, *11*(24), 3011. https://doi.org/10.3390/rs11243011

Pitman, A. J. (2003). The evolution of, and revolution in, land surface schemes designed for climate models. *International Journal of Climatology*, *23*(5), 479–510. https://doi.org/10.1002/joc.893

Richardson, A. D., Aubrecht, D. M., Basler, D., Hufkens, K., Muir, C. D., & Hanssen, L. (2021). Developmental changes in the reflectance spectra of temperate deciduous tree leaves and implications for thermal emissivity and leaf temperature. *New Phytologist*, *229*(2), 791–804. https://doi.org/10.1111/nph.16909

Sellers, P. J., Dickinson, R. E., Randall, D. A., Betts, A. K., Hall, F. G., Berry, J. A., et al. (1997). Modeling the exchanges of energy, water, and carbon between continents and the atmosphere. *Science*, *275*(5299), 502–509. https://doi.org/10.1126/science.275.5299.502

Sellers, P. J., Mintz, Y., Sud, Y. C., & Dalcher, A. (1986). A simple biosphere model (SIB) for use within general circulation models. *Journal of the Atmospheric Sciences*, *43*(6), 505–531. https://doi.org/10.1175/1520-0469(1986)043<0505:asbmfu>2.0.co;2

Sutherland, R. A. (1986). Broadband and spectral emissivities (2–18 μm) of some natural soils and vegetation. *Journal of Atmospheric and Oceanic Technology*, *3*(1), 199–202. https://doi.org/10.1175/1520-0426(1986)003<0199:baseos>2.0.co;2

Van de Griend, A., & Owe, M. (1993). On the relationship between thermal emissivity and the normalized difference vegetation index for natural surfaces. *International Journal of Remote Sensing*, *14*(6), 1119–1131. https://doi.org/10.1080/01431169308904400

Verseghy, D. (2012). CLASS–the Canadian land surface scheme (version 3.6). *Environment Canada Science and Technology Branch Technical Report*, 176.

19422466, 2024, 9, Downloaded from https://agupubs.onlinelibrary.wiley.com/doi/10.1029/2023MS003957 by Ewha Womans University Library, Wiley Online Library on [04/03/2025]. See the Terms and Conditions (https://onlinelibrary.wiley.com/terms-and-conditions) on Wiley Online Library for rules of use; OA articles are governed by the applicable Creative Commons License

Wan, Z., Hook, S., & Hulley, G. (2021). MODIS/Terra land surface temperature/emissivity monthly L3 global 0.05Deg CMG V061(MOD11C3) [Dataset]. *NASA EOSDIS Land Processes Distributed Active Archive Center*. https://doi.org/10.5067/MODIS/MOD11C3.061

Wang, Y. P., Kowalczyk, E., Leuning, R., Abramowitz, G., Raupach, M. R., Pak, B., et al. (2011). Diagnosing errors in a land surface model (CABLE) in the time and frequency domains. *Journal of Geophysical Research*, *116*(G1), G01034. https://doi.org/10.1029/2010jg001385

Williams, M., Rastetter, E. B., Fernandes, D. N., Goulden, M. L., Wofsy, S. C., Shaver, G. R., et al. (1996). Modelling the soil-plant-atmosphere continuum in a Quercus–Acer stand at Harvard Forest: The regulation of stomatal conductance by light, nitrogen and soil/plant hydraulic properties. *Plant, Cell and Environment*, *19*(8), 911–927. https://doi.org/10.1111/j.1365-3040.1996.tb00456.x

Zhao, M., Golaz, J., Held, I. M., Guo, H., Balaji, V., Benson, R., et al. (2018). The GFDL global atmosphere and land model AM4.0/LM4.0: 2. Model description, sensitivity studies, and tuning strategies. *Journal of Advances in Modeling Earth Systems*, *10*(3), 735–769. https://doi.org/10.1002/2017ms001209

Zhou, L., Dickinson, R. E., Tian, Y., Jin, M., Ogawa, K., Yu, H., & Schmugge, T. (2003). A sensitivity study of climate and energy balance simulations with use of satellite-derived emissivity data over Northern Africa and the Arabian Peninsula. *Journal of Geophysical Research*, *108*(D24), 4795. https://doi.org/10.1029/2003jd004083

19422466, 2024, 9, Downloaded from https://agupubs.onlinelibrary.wiley.com/doi/10.1029/2023MS003957 by Ewha Womans University Library, Wiley Online Library on [04/03/2025]. See the Terms and Conditions (https://onlinelibrary.wiley.com/terms-and-conditions) on Wiley Online Library for rules of use; OA articles are governed by the applicable Creative Commons License